

Experimental Investigation
of Generic Three-Dimensional
Sidewall-Compression
Scramjet Inlets at Mach 6
in Tetrafluoromethane

Scott D. Holland
Langley Research Center
Hampton, Virginia

(NASA-TM-4497) EXPERIMENTAL
INVESTIGATION OF GENERIC
THREE-DIMENSIONAL
SIDEWALL-COMPRESSION SCRAMJET
INLETS AT MACH 6 IN
TETRAFLUOROMETHANE (NASA) 47 P

N94-23339

Unclass

H1/34 0201557



National Aeronautics and
Space Administration

Office of Management

Scientific and Technical
Information Program

1993

Abstract

Three-dimensional sidewall-compression scramjet inlets with leading-edge sweeps of 30° and 70° have been tested in the Langley Hypersonic CF_4 Tunnel at Mach 6 with a ratio of specific heats of 1.2. The parametric effects of leading-edge sweep, cowl position, contraction ratio, and Reynolds number were investigated. The models were instrumented with 42 static pressure orifices that were distributed on the sidewalls, baseplate, and cowl. Schlieren movies were made of selected tunnel runs for flow visualization of the entrance plane and cowl region. Although these movies could not show the internal flow, the effect of the internal flow spillage on the external flow was evident. To obtain an approximate characterization of the flow field, a modification to two-dimensional, inviscid, oblique shock theory was derived to accommodate the three-dimensional effects of leading-edge sweep. This theory qualitatively predicted the reflected shock structure (i.e., sidewall impingement locations) and the observed increase in spillage with increasing leading-edge sweep. The primary effect of moving the cowl forward was capturing the flow that would have otherwise spilled ahead of the cowl. Increasing the contraction ratio (moving the sidewalls closer together) increases the number of internal shock reflections and hence incrementally increases the sidewall pressure distribution. Significant Reynolds number effects were noted over a small range of Reynolds number.

Introduction

The requirement for supersonic combustion ramjets for high Mach number propulsion of airbreathing vehicles such as the National Aero-Space Plane (X-30) has been recognized (refs. 1 and 2). Such propulsion systems are highly integrated with the airframe to exploit the compression effected by the forebody bow shock. (The advantages of propulsion-airframe integration have been well recognized for many years. See ref. 3.) The precompression of the flow in the vertical direction upstream of the engine inlet is demonstrated in figure 1. It is anticipated that the boundary layer at the inlet entrance on a full-scale hypersonic vehicle would be large with respect to the inlet height. (Computational results have been presented in ref. 4 for inflow boundary layers as large as 20 percent of the inlet height.) As a result, further turning in the vertical direction, as in two-dimensional inlets, would greatly increase the probability of large-scale separation regions at the entrance of the inlet as a result of the shock boundary-layer interaction. It is important to note that the scale and nature of these interactions

depend strongly upon whether the boundary layer is laminar, transitional, or turbulent; the inflow boundary layer for this series of tests is laminar.

The sidewall compression inlet (fig. 2) represents a three-dimensional configuration wherein internal flow compression is accomplished in the horizontal direction by wedge-shaped sidewalls that reduce the total vertical turning that the flow must encounter to obtain the desired pressure rise. The leading edges of these sidewalls are swept to reduce aerothermal loads, hence cooling requirements on the leading edge, and to increase inlet flow spillage, which aids in starting the fixed geometry inlet at the lower Mach numbers. The aft sweep has the effect of turning the flow away from the forebody plane (spilling out ahead of the cowl); as the Mach number is increased, the sidewall shock angles become smaller, which effectively reduces the spillage window and increases the mass capture (ref. 5).

Three-dimensional sidewall-compression scramjet inlet models with leading-edge sweep angles of 30° and 70° have been tested in the Langley Hypersonic CF_4 Tunnel at Mach 6 with a free-stream ratio of specific heats of 1.2. The models were instrumented with static pressure orifices distributed on the sidewalls, baseplate, and cowl to quantify the effects of cowl position, contraction ratio, and Reynolds number. Schlieren movies were made of selected runs for flow visualization.

This report identifies inlet characteristics in tetrafluoromethane (CF_4) as a first step toward obtaining a characterization of simulated real-gas effects on inlet flow fields. Traditionally, CF_4 has been used for blunt-body research (refs. 6-8) to simulate the decrease in the ratio of specific heats γ that occurs within a dissociating shock layer surrounding a vehicle that is reentering the atmosphere. The direct effect of a decreased γ is an increase in the normal-shock density ratio, which has been shown to be a primary factor in determining the inviscid characteristics of the hypersonic flow surrounding a reentering vehicle. Midden and Miller (ref. 9) point out that for relatively slender bodies and lifting bodies, the simulation of low γ effects is approximate because of the variation of γ within the shock layer along or around a reentering vehicle, which is in contrast to the nearly constant γ within the shock layer in CF_4 . In spite of this effect, they note the importance of such tests in providing a lower bound for the assessment of γ effects, which cannot be obtained in other ground test facilities. To obtain the explicit effects of low γ , the model must be tested in both CF_4 and air. This report is a first step toward that end. Further, these tests may be considered exploratory, because

these models were the largest tested to date in the CF₄ facility. It was therefore not known if the tunnel could remain started once the model was injected into the flow. Finally, although the instrumentation density in these tests was insufficient for a true computational fluid dynamics (CFD) validation, this test in CF₄ provides a set of data that may be used to compare with CFD calculations for a virial gas. The complete data set (which included descriptions of the models, facility, and testing methods, the test matrix and run log, and numerous data tables, line plots, and schlieren photographs) was released for reference without analysis in reference 10. The present work presents a subset of those data to provide a concise analysis and discussion.

Symbols

Values are given in U.S. Customary Units, but they are occasionally given in SI Units or in both units where they are considered useful.

CR	contraction ratio, W/g
g	throat gap, in.
H	height of inlet, 2.75 in.
h	enthalpy, J/kg (Btu/lbm)
M	Mach number
M_{1n}	component of free-stream Mach number normal to leading edge (see fig. 21)
M_{1p}	component of free-stream Mach number parallel to leading edge (see fig. 21)
M_{2n}	postshock component of Mach vector normal to leading edge in plane of wedge (see fig. 21)
M_{2p}	postshock component of Mach vector parallel to leading edge in plane of wedge (see fig. 21)
N_{Pr}	Prandtl number
N_{Re}	Reynolds number
p	pressure, Pa (psia)
q	dynamic pressure
T	temperature, K (°R)
T'_x	distance from sidewall leading edge to throat, 5.04 in.
u	velocity, m/sec (ft/sec)

W	inlet width at sidewall leading edge, in.
x	axial distance measured from baseplate leading edge (see fig. 4), in.
x'	local axial distance measured from sidewall leading edge (see fig. 4), in.
y	vertical distance from bottom surface (see fig. 4), in.
Z	compressibility factor
z	lateral distance from inlet plane of symmetry (see fig. 4), in.
β, Γ	angles measured in plane of wedge (see fig. 21), deg
γ	ratio of specific heats
δ	sidewall-compression angle, deg
δ_{eff}	effective sidewall-compression angle, measured normal to sidewall leading edge, deg
ζ	spillage angle (see fig. 21), deg
η_{ke}	kinetic energy efficiency
θ_{eff}	effective oblique shock angle, measured normal to sidewall leading edge, deg
Λ	leading-edge sweep angle, deg
μ	viscosity, N-sec/in ² (lbm/ft-sec)
ρ	density, kg/m ³ (lbm/ft ³)
Subscripts:	
t	total conditions
1	wind-tunnel free-stream conditions
2	postshock conditions

Experimental Methods

Model Description

Photographs of the inlet models are shown in figure 3, and sketches are presented in figure 4. Sidewall leading-edge sweeps of 30° and 70° were selected to represent both moderately and highly swept models. The generic, three-dimensional sidewall-compression inlets used in the present report have been under study for several years. A review of the development of scramjet research at Langley Research Center is presented in reference 11; much of the inlet work devoted to that effort was reported in references 12–16. As a result of a trade study (ref. 14), the sidewall-compression angle was fixed at 6°. This angle was a

compromise between larger compression angles (leading to stronger internal shocks with increased probability of boundary-layer separation) and smaller compression angles (leading to weaker internal shocks but requiring the inlet to be longer to obtain the same compression, and thus imposing a size and weight penalty on the inlet). The models were 2.75 in. tall and were machined of aluminum; the sidewalls had leading-edge diameters of 0.010 in., and the baseplate and cowl each had leading-edge diameters of 0.015 in. with 10° of external compression. The models were injected into the tunnel in an inverted orientation, with the cowl on top. The vehicle forebody plane was represented by a flat plate and will be referred to as the *baseplate*. The model was uncooled. Because the forebody boundary layer was not modeled, the configuration was said to be uninstalled.

The 30° sidewall model was originally designed for a parametric study of inlet starting performance (ref. 15) and was instrumented only to the extent necessary to determine if unstart had occurred. A number of pressure taps were added to the 30° model, a 70° leading-edge sweep model was fabricated, and both were tested in the Langley 22-Inch Mach 20 Helium Tunnel (ref. 16). Because these models were adapted from previous test programs, the number and location of the instrumentation were not optimal. Static pressure orifices (with 0.040-in. inside diameters) were arranged in single arrays located along the centerlines of the baseplate, sidewall, and cowl, and also on the sidewall at $y/H = 0.13$ (near the baseplate) and $y/H = 0.87$ (near the cowl), as shown in figure 4.

The contraction ratio is defined as the ratio of the inlet entrance area to the throat area. Because the present configuration is characterized by a constant height, the contraction ratio reduces to the ratio of the inlet entrance width W to the throat gap g . (See fig. 4.) This ratio can be varied between the runs by laterally moving the sidewalls. The cowl position can also be changed between runs. For the present study, the cowl was placed at the throat (referred to as *0-percent cowl*) and forward of the throat 25 percent of the distance between the throat and the sidewall leading edge (referred to as *25-percent cowl*). The axial distance down the sidewalls x' is nondimensionalized by the distance between the sidewall leading edge and the throat entrance T'_x for comparison of pressure distributions for configurations with different leading-edge sweeps (i.e., the equation $x'/T'_x = 0.30$ represents an axial location 30 percent of the throat length downstream of the sidewall leading edge, regardless of the leading-edge sweep).

Facility Description

Since these tests were made, the Langley Hypersonic CF₄ Tunnel has undergone major upgrades. A description of the upgraded facility is presented in reference 17, and a detailed description of the facility as it existed at the time of these tests is presented in reference 9. The important features of the original tunnel that pertain to these tests are noted herein. Figure 5 is a schematic of the original tunnel; this schematic shows the major components. The high-pressure supply system consisted of a CF₄ storage trailer rated for 2500 psia, a compressor capable of 5000 psia, a 5000-psia bottle field with a storage volume of 120 ft³, and an externally loaded dome pressure regulator to control the operating pressure of the tunnel. After compression, the gas was heated to a maximum temperature of 1500°R as it flowed through 44 spirally wound stainless steel tubes immersed in two parallel lead-bath heaters. Particles larger than 10 μ m were removed from the flow by an in-line filter located between the heater and the settling chamber. The flow was then expanded through a contoured, axisymmetric nozzle with a 0.446-in-diameter throat, that was designed to create Mach 6 flow at the nozzle exit (approximately 20 in. in diameter). The flow exhausted into an open-jet test section approximately 6 ft in length and 5 ft in diameter, was collected by a diffuser, and was then cooled by a water-cooled heat exchanger before being dumped into vacuum spheres. The spheres had a combined total volume of 72 000 ft³. These spheres were then evacuated into a reclaimer system.

Prior to a run, the test section, nozzle, settling chamber, and vacuum spheres were evacuated to approximately 0.01 psia. The dome loader was set to the desired reservoir pressure, and the heaters were set to the desired flow temperature. An automated sequencer opened and closed appropriate valves and controlled the injection and retraction of the model. Although run times up to 30 sec are possible, a run time of 15 sec was adequate for these tests.

Instrumentation

The settling chamber (reservoir) pressure $p_{t,1}$ was measured with strain-gage pressure transducers that have full-scale ratings of either 3000 or 300 psia, depending on the operating condition of the tunnel. The settling chamber (reservoir) temperature $T_{t,1}$ was measured with two chromel-alumel thermocouples inserted through the wall of the settling chamber and positioned near the center of the chamber. The pitot pressure of the flow in the test section $p_{t,2}$ was measured by a flat-faced cylindrical probe that was mounted in the test section and linked to an

electronically scanned pressure (ESP) silicon sensor module. A second ESP module was used to measure the surface pressures on the model. Each 2.5-psid ESP module contained 32 sensors and was located at the base of the model strut to minimize the tubing length between the pressure orifices on the model and the module. The pressure tubing and ESP modules were insulated to prevent thermal shift of the ESP calibration. An *in situ* calibration consisted of applying three known pressures (vacuum levels) that were chosen to span the range of the expected measured pressures. A sample rate of 20 samples per second was obtained for the 64 channels.

Schlieren movies were made for flow visualization in the region of the entrance plane and cowl, and they were recorded on 16-mm video news film. The movies were shot at 128 frames/second; therefore, the flow could be observed on an 8-msec time scale.

Test Conditions

Tests were performed at a nominal Mach number of 6 for reservoir pressures of 300, 1000, and 2000 psia at a reservoir temperature of 1200°R. The test matrices for the two models are given in tables 1 and 2. Free-stream and postnormal-shock flow properties were calculated as outlined in reference 9. The nominal free-stream Reynolds numbers obtained under these conditions were 0.89×10^5 , 2.89×10^5 , and 5.50×10^5 per foot, respectively. Free-stream static pressures were quite low: 0.01 psia, 0.03 psia, and 0.05 psia, respectively. The free-stream ratio of specific heats was 1.2. Tables of free-stream and postnormal-shock flow properties are provided for the three Reynolds numbers in tables 3–5. A list of tunnel runs correlating the test conditions, model configurations, and run numbers is given in table 6.

Pitot-rake surveys of the flow in the test section were performed previously for reservoir pressures from 100 to 400 psia and 1000 to 2500 psia (ref. 9). Each of the surveys showed a uniform core but with a centerline disturbance. At the lower reservoir pressures, a second disturbance was located at a radius of 4 in. from the centerline. Because the model was only 2.75 in. tall, it was injected 1 in. above the centerline, so that injection of either disturbance was avoided. The diameter of the core varied weakly with reservoir pressure from 14 in. at 300 psia to 15 in. at 2000 psia. In each case, the model was completely immersed in the core, free from tunnel boundary-layer interference.

Data Reduction and Uncertainty

Measured values of $p_{t,1}$ and $T_{t,1}$ are believed to be accurate to within 2 percent (ref. 9). Values of p/p_1 are estimated to be accurate to within 4 percent, based on manufacturer specifications for the given pressure levels. Run-to-run repeatability was examined for two configurations. The mean absolute deviation of the set of measured pressures for both configurations was less than 4 percent; hence, it was less than the uncertainty of the measurement.

Test Medium

In 1969, Jones and Hunt (ref. 6) pointed out that the purpose of the CF₄ Tunnel was to provide a conventional wind tunnel that could simulate the increased normal-shock density ratios (from 10 to 20) and the decreased ratio of specific heats (as low as 1.1) encountered in hypervelocity flight because of the chemical dissociation of the postshock flow. In 1981, Sutton (ref. 18) indicated that conventional air or nitrogen tunnels were limited to $\gamma = 1.4$ and a density ratio of approximately 6 and that helium tunnels are limited to $\gamma = 1.67$ and a normal-shock density ratio of 4; however, they showed that the CF₄ Tunnel provides a normal-shock density ratio of 12 with $\gamma < 1.4$. The thermodynamic and transport properties of CF₄ may be found in references 19–21, and relations are presented in a form amenable to flow-field computer codes in reference 18. Although the relations must generally account for intermolecular force effects and high-temperature effects, in the test section the gas has been expanded to such a low pressure that intermolecular force effects and high-temperature effects are negligible in both the free stream and behind a normal shock. For these tests, therefore, CF₄ can be treated as thermally perfect ($Z = 1$) and calorically imperfect, with the specific heats given as functions of temperature only (ref. 18).

Results and Discussion

As previously noted, a preliminary data release for these tests is presented in reference 10. Tabular pressure data for each run were provided along with numerous plots that cross-plotted the effects of leading-edge sweep, cowl position, contraction ratio, and Reynolds number for every set of configurations for which cross-plotting was possible. The present report presents a typical subset of those data to provide a concise analysis and discussion. A discussion of the shock structure predicted by an inviscid approximate analysis is presented first to serve as a framework for the analysis of the experimental data.

Inviscid Analysis

When the flow encounters the wedge-shaped sidewalls, a complex shock structure develops. Consider first the inviscid flow past a pair of infinitely tall, unswept (two-dimensional) wedges located opposite one another (i.e., an unswept inlet of infinite height, fig. 6). A pair of shock sheets extend from the leading edge of the wedges, cross at the centerline, and then impinge on the sidewalls. These shocks cancel if they are incident at the shoulder in the throat; otherwise, they continue to reflect if they strike upstream of the shoulder. Figure 6 illustrates the three possibilities: shock aft of shoulder, shock on shoulder, and shock upstream of shoulder. This reflected shock pattern has been demonstrated computationally for viscous flow through a sidewall-compression inlet of similar design in Mach 5 air (perfect gas) for a leading-edge sweep of 45° (ref. 22). Although the flow conditions were different, the prominent features of the flow are expected to be similar to the present configuration. From a geometric standpoint, the addition of a leading-edge sweep to the sidewalls causes the shock sheets that are generated by the leading edge, the line along which the shocks intersect on the centerline, and the line along which the reflected shocks impinge on the sidewalls to be swept at the leading-edge sweep angle. In the absence of three-dimensional end effects, shock interactions of this nature occur along lines of constant leading-edge sweep angle (provided the shock waves are attached). This trend was also demonstrated computationally (see, e.g., figs. 5 and 6 of ref. 22). Hence, figure 6 illustrates the approximate, inviscid model for cross sections of both swept and unswept inlets.

The internal shock pattern is largely dictated by the sidewall-compression angle δ , the inflow Mach number M_1 , and the contraction ratio CR. The sidewall-compression angle and the inflow Mach number determine the inviscid shock angle through oblique shock theory. The addition of leading-edge sweep alters the application of the theory as given in the appendix. For a fixed sidewall-compression angle and Mach number (and hence fixed shock angles), the location of the shock impingement point is determined by the contraction ratio (distance between the sidewalls). Thus, increasing the contraction ratio (bringing the sidewalls closer together) increases the compression of the inlet by causing the internal flow to encounter a greater number of reflected oblique shocks. Results from the computation of the internal reflected oblique shocks inside the 30° and 70° leading-edge sweep models via the equations presented in the appendix are given in table 7. A scale drawing of the shock structure for the $\Lambda = 30^\circ$ config-

uration for CR = 3, 5, and 9 is presented in figure 7. All three contraction ratios can be superimposed on the same figure, because an increase in contraction ratio yields a decrease in the distance between the sidewall and the centerline; hence, three centerlines are drawn. The change in contraction ratio does not affect the shock angles, but does affect the distance the shocks travel to interact at the centerline. Table 7 also shows that the shocks in the 70° model detach upstream of the throat. The equations presented in the appendix show that the $\Lambda = 70^\circ$ configuration has a significantly larger effective sidewall-compression angle δ_{eff} than the 30° model. The combination of increased δ_{eff} and decreased M_{1n} (ref. 5) for the same inflow Mach number causes the component of the Mach vector normal to the reflected shock sheet to fall below 1.0 after fewer shocks for $\Lambda = 70^\circ$ than for $\Lambda = 30^\circ$. This fall results in the detached shock reflection.

Sweeping the leading edges aft has an additional effect of turning the flow away from the baseplate toward the cowl as the flow passes through the swept shocks. This flow deflection is shown three-dimensionally behind the first shock in figure 8. (The flow deflection behind subsequent shocks is not shown.) The appendix presents equations to compute the inviscid flow deflection (spillage) angle ζ between two infinitely long swept wedges (i.e., neglecting end effects) with this modified oblique shock theory. The spillage angle is on the order of a few degrees and is increased incrementally by each reflected shock (i.e., ζ for region 3 of fig. 6 is greater than ζ for region 2). The complexity of computing spillage angles behind subsequent shocks is illustrated in the figures for appendix A of reference 14.

Upstream of the cowl leading edge, the flow that is deflected away from the baseplate spills from the inlet. This spillage is important in helping the inlet start at lower Mach numbers. As the Mach number is increased, the area (in the plane of the cowl) behind the shock sheets is decreased, because the shocks lie closer to the sidewalls (fig. 9). The smaller shock angles effectively reduce that spillage window and increases the mass capture of the inlet, so that the inlet is more efficient at high Mach numbers. It has also been demonstrated inviscidly (ref. 5) that as the Mach number is increased, the deflection of the flow toward the cowl is decreased, which also serves to improve the mass capture at higher Mach numbers. It is these characteristics that make it possible to consider a fixed-geometry inlet for use over a wide Mach number range. Compared with an aft placement, the cowl forward configuration captures more of the mass that would have otherwise

spilled. It is expected that a shock will develop on the cowl leading edge inside the inlet as the deflected flow impinges on the cowl and is turned back parallel to the cowl surface.

For inlets of finite height, end effects can play a large role in determining the internal flow characteristics of the inlet. When the inlet height is small compared with the width, the present modification to oblique shock theory does not adequately account for the behavior of the flow. Upstream of the cowl leading edge, spillage tends to cause a pressure relief near the cowl plane and yields lower pressures than would be expected by the modified oblique shock theory. The existence of a centered expansion that originates from the interface of the shock sheet and baseplate (fig. 10) was hypothesized in reference 23. The hypothesized centered expansion would ensure that the flow vector downstream of the shock sheet lies not only in the plane of the flow turned toward the cowl but also in the plane of the baseplate. The centered expansion hypothesis permits the flow vector to be positioned in both planes and predicts pressures near the baseplate to be lower than in the center of the inlet, where end effects are of lesser importance. Although this theory provides an interesting inviscid model of the flow, it fails to capture the true complexity of the corner flow interactions and the effects of the induced crossflow at the symmetry plane. The instrumentation density in the present set of models is insufficient to adequately address these topics in the present paper, except as deviations from the inviscid results for infinitely tall swept wedges. However, corner flow interactions have been addressed in reference 24, a double-fin interaction has been presented at Mach 4 in reference 25, and experimental and computational results of the induced crossflow interactions in an inlet at Mach 10 have been presented in reference 26.

Schlieren Movies

Schlieren movies of the entrance plane and cowl region showed that the flow was steady on an 8-msec time scale. When combined with the pressure measurements, these movies indicated that the inlet started for each configuration tested and remained started for the duration of the test. Although these movies could not detail the internal flow features, the effects of the internal flow on the external flow in terms of spillage were evident.

The modified oblique shock theory presented in the appendix predicts that the spillage angle increases with leading-edge sweep angle. (See ref. 5.) Thus, the spillage is expected to be greater for $\Lambda = 70^\circ$ than for $\Lambda = 30^\circ$. Figures 11(a) and (b)

are enlarged frames taken from the schlieren movies for $\Lambda = 30^\circ$ and 70° , respectively, at $CR = 5$, 0-percent cowl, and $N_{Re} = 5.50 \times 10^6$ per foot. The view, which is a profile of the inlet, is shown in an inverted orientation (relative to flight) with the cowl on top. A small quantity of silicone sealant was placed on the external surface of the cowl to protect the pressure tubing leading from the cowl. A bow shock is visible as a result of the silicone sealant, but it is located far enough downstream of the cowl leading edge that it does not appear to interfere with the flow into the inlet. (In fig. 11(b), this feature is out of the field of view.) The schlieren photographs present an integrated view across the span of the inlet. Two-dimensional features (i.e., features that are constant across the width of the inlet), such as the shocks on the underside of the baseplate, appear in sharp detail. Because of the horizontal orientation of the knife edge in the schlieren system, increases in density (shocks) appear dark in the top half of the frame. Interpretation of the schlieren image in the region above the inlet is complicated by the fact that the shock waves are skewed relative to the plane of the schlieren. The model of the flow field based on the inviscid analysis presented in figure 8, where the flow deflected toward the cowl by the sidewall leading-edge shocks in the first shock bay (region 2 of fig. 6), is shown three-dimensionally, and the spillage angle ζ is identified. (Also, the flow deflection in region 3, although greater than for region 2, is not shown.) When the inlet is viewed in profile, only the underside of the internal shock sheet, which extends beyond the cowl plane, is visible. This feature was faint in the schlieren movie of the 30° model and did not reproduce well in figure 11(a). Because of the increased spillage with increased leading-edge sweep, this feature is more distinct for the $\Lambda = 70^\circ$ configuration (fig. 11(b)). (The improved definition in the schlieren photographs of the $\Lambda = 70^\circ$ configuration was observed for all configurations; figs. 11(a) and (b) present typical results.) The dark region above the cowl plane in the schlieren photograph appears to extend aft of the leading edge to approximately 37 percent of the distance to the throat. Modified oblique shock theory indicates that the internal-sidewall leading-edge shocks should reach the inlet centerline (i.e., point B of fig. 8) at $x'/T_x' = 0.41$ (41 percent of the distance to the throat). Thus, the dark regions above the inlet likely result from the internal shocks. Because there are more than one shock bay upstream of the cowl leading edge, subsequent dark regions in the schlieren photographs are observed. Also, the position of the cowl had little influence on the global external flow field. A complete set of schlieren photographs is presented in

reference 10. However, significant degradation of the image quality occurred in the conversion of the 16-mm video frame to a 4- by 5-in. negative of the photographs in the report.

Pressure Data

A discussion of the pressure distributions on the 30° model are presented first. Plots that superimpose the pressure distributions on all surfaces of a given configuration are designated "configuration-complete" plots and are discussed with respect to the overall flow structure. The effect of the cowl position for a given contraction ratio is discussed next, and the contraction-ratio effects for a typical cowl position are then presented. A similar format is followed for the 70° model. Finally, discussions of the leading-edge sweep and Reynolds number effects are presented.

30° model. Figures 12(a)–(c) are configuration-complete plots for $\Lambda = 30^\circ$ with 0-percent cowl, $N_{Re} = 5.50 \times 10^5$ per foot, and CR = 3, 5, and 9, respectively. The centerline sidewall pressure distribution in figure 11(a) reveals a sharp rise at $x'/T'_x \approx 0.85$. The modified oblique shock theory predicts the leading-edge shocks to cross at the centerline and impinge on the sidewall at $x'/T'_x \approx 0.91$ for CR = 3. (See table 7.) There is a sharp dip in the pressure as the flow expands around the shoulder into the constant-area throat region ($x'/T'_x = 1.0$); then there is a rise as a result of the reflected shock impingement. Aft of the throat exit, the model sidewalls diverge to reexpand the flow, and this expansion is noted in the sidewall centerline pressure distribution. The pressure distribution on the sidewall near the baseplate ($y/H = 0.13$) follows the same trend but slightly below the centerline curve, which agrees with the inviscid shock-expansion model of reference 23. Additionally, the sidewall at $y/H = 0.87$ benefits from a pressure relief as a result of the inlet spillage and also falls slightly below the centerline sidewall curve. Figure 11(b) represents the same configuration but with a contraction ratio of 5. The sharp sidewall centerline pressure rise has moved forward to $x'/T'_x \approx 0.7$, which indicates that the shock impingement point has moved forward with the increasing contraction ratio (decreasing throat gap). Figure 6 demonstrates this impingement point movement two-dimensionally. The modified oblique shock theory predicts the impingement location to be at $x'/T'_x = 0.76$. While the higher contraction ratio yields a higher internal pressure in the inlet, the same trend of compression-expansion-compression is shown in the throat. However, the shock impingement locations have changed. Again, the pressures

at $y/H = 0.13$ and 0.87 are slightly lower than the sidewall centerline pressure. This is likewise true of the sidewall for a contraction ratio of 9 (fig. 12(c)). Because of the increase in contraction ratio, a greater number of internal shocks are encountered upstream of the throat. Individual shock impingements are not resolved in the sidewall pressure distributions, but the pressure levels upstream of the throat are higher than for CR = 3 or 5. The previously noted dip in the sidewall centerline pressure distribution at the beginning of the throat is not present; rather, the pressure rises throughout the throat region. The spatial resolution provided near the beginning of the throat is insufficient to indicate whether or not an expansion exists locally; however, if the expansion pattern exists, its influence is more restricted by the proximity of the repeated shock impingements. That is, modified oblique shock theory predicts shock impingements of the sidewall first at $x'/T'_x = 0.68$ and then at $x'/T'_x = 0.93$ and 1.03 . Because the displacement of the sidewall boundary layer tends to move these impingements forward, it is possible that a shock-on-shoulder condition exists for this configuration.

Figures 13(a)–(e) compare the effect of the cowl position on pressures measured on the baseplate, the sidewall centerline, the sidewall at $y/H = 0.87$ and $y/H = 0.13$, and the cowl at CR = 3, $\Lambda = 30^\circ$, and $N_{Re} = 5.50 \times 10^5$ per foot. These plots are typical of the data taken at each contraction ratio. The plots reveal that the baseplate centerline, the sidewall at $y/H = 0.13$, and the sidewall centerline appear to be out of the domain of influence of the cowl. For the cases of no cowl and 0-percent cowl (aft cowl position), the sidewall pressures at $y/H = 0.87$ (fig. 13(d)) steadily increase as a result of the shock impingement and then decrease because of the local expansion around the shoulder at the throat. For the forward (25 percent) cowl position, however, the effects of the local expansion appear to be dominated by a pressure increase caused by the internal cowl leading-edge shock. This pressure increase is evident at each pressure orifice at the $y/H = 0.87$ station. This shock occurs as the flow impacts the free-stream aligned cowl at some angle of incidence and is turned back parallel to the cowl. The cowl centerline data (fig. 13(e)) demonstrates that the location of the cowl with respect to the pockets of flow deflected toward the cowl plane influences the pressure on the cowl. With the cowl in the aft (0-percent) position, much of the high-pressure fluid that would have been captured by the 25-percent cowl configuration has spilled ahead of the cowl, and there is a lower pressure on the cowl than for the 25-percent position. The

pressure relaxation in the throat region previously noted at the sidewall centerline is also evident in the cowl data for its aft placement.

The effects of contraction ratio are presented for a 0-percent cowl, $N_{Re} = 5.50 \times 10^5$ per foot configuration in figures 14(a)–(e) and represent trends typical of the data recorded. These figures demonstrate the effects of contraction ratio on the static pressures on the baseplate, the sidewall centerline, the sidewall at $y/H = 0.13$ and $y/H = 0.87$, and the cowl, respectively. Figure 14(a) reveals that the effect of increasing contraction ratio (bringing the sidewalls closer together) yields an overall increase in the pressure distribution. The baseplate boundary layer is observed from schlieren photographs to generate a weak shock at the baseplate leading edge. This boundary layer and its associated shock seem to disperse the sharp pressure peaks (predicted by the modified oblique shock theory), where the sidewall shocks intersect at the centerline. Figure 14(b) presents the contraction-ratio effects on the sidewall centerline pressure distribution. The change in contraction ratio produces a change in the incident shock location, which is predicted approximately by the modified oblique shock theory. The change in shock location also influences the total compression of the inlet in that a more forward incidence location allows more shock reflections between the leading edge and the throat, each of which incrementally increases the static pressure in the inlet. Again, at the highest contraction ratio, the local expansion at the shoulder in the throat is not resolved. The overall increase in pressure with contraction ratio is also noted on the sidewalls at $y/H = 0.13$ and at $y/H = 0.87$ (figs. 14(c) and (d)). The cowl pressures (fig. 14(e)) also demonstrate a strong dependence on contraction ratio; this dependence varies by as much as a factor of 4 over the range of contraction ratios tested.

70° model. Figures 15(a)–(c) are configuration-complete plots for the 70° leading-edge sweep, $N_{Re} = 5.5 \times 10^5$ per foot, 0-percent cowl configuration at contraction ratios of 3, 5, and 9, respectively. (Cowl pressures are not provided for the 70° configuration because the cowl pressure orifices were located aft of the constant-area throat exit.) As with the 30° data, the sidewall pressure distribution at $y/H = 0.13$ is lower than the centerline; this trend is in agreement with the aforementioned shock-expansion model. The sidewall centerline array of pressure orifices is sparse leading up to the throat, so the reflected shock patterns are not resolved. Although the pressure at the shoulder of the throat was measured, the peak pressure on the inlet sidewalls

cannot be determined; it is possible that the peak has occurred between orifices. The sidewall centerline pressure distribution for CR = 3 shows the previously noted compression-expansion-compression pattern, despite the fact that the modified oblique shock theory for $\Lambda = 70^\circ$ predicts internal shock detachment upstream of the throat for each of the contraction ratios tested. Even the inviscid flow structure downstream of the shock detachment is complex and does lend itself to simple analysis. In this situation, a full three-dimensional Navier-Stokes CFD solution is desirable to more fully define the flow field.

The schlieren photographs show and the modified oblique shock theory predicts higher spillage for the 70° configuration than for the 30° configuration. The sparseness of the pressure orifices upstream of the predicted shock detachment precludes comment on whether the 70° model yields a pressure relief near the cowl as a result of flow spillage such as was noted with the 30° configuration. (However, fig. 15(a) shows a higher pressure upstream of the throat at $y/H = 0.87$ rather than at the sidewall centerline.) Particularly at the higher contraction ratios (figs. 15(b) and (c)), the data at the sidewall centerline and at $y/H = 0.87$ show a strong pressure relaxation in the throat without the appearance of pressure rises associated with reflected shocks.

Figures 16(a)–(d) present the effects of the cowl position on pressures measured on the baseplate, the sidewall centerline, and the sidewall at $y/H = 0.87$ and 0.13 for the 70° model at a contraction ratio of 3 and $N_{Re} = 5.50 \times 10^5$ per foot. (This is the same model configuration that was used for the presentation of cowl position effects for the 30° model.) These plots are typical of the data taken at each contraction ratio, and they reveal that the baseplate, the sidewall at $y/H = 0.13$, and the sidewall centerline are out of the domain of influence of the cowl. With no cowl and 0-percent cowl (aft cowl position), the sidewall pressures at $y/H = 0.87$ are not influenced by the cowl position; the pressures increase toward the throat and then expand around the shoulder. However, for the 25-percent cowl configuration, the pressure relief at $y/H = 0.87$ observed in the throat as a result of the expansion is reduced; this reduction may possibly be caused by the crossing of the cowl shock just upstream of these orifices. Although no cowl data are presented for the 0-percent position (because the orifices are located aft of the constant-area throat exit), figure 16(e) presents the cowl pressure distribution for the 25-percent cowl configuration. Pressures on the cowl are high, and although the internal reflecting shock model is no longer valid from an

inviscid perspective, the pressures on the cowl continue to rise toward the throat. Even if the shock sheets have become detached, spillage is expected because of the large pressure difference between the free-stream and the internal flows. When the cowl is moved forward to block some of this spillage, high cowl pressures result from the impingement of this flow on the cowl.

Contraction-ratio effects are examined on the 70° model at a 0-percent cowl and a free-stream Reynolds number of 5.50×10^5 per foot; these results were typical of the data at each cowl position. (The contraction-ratio effects for the 70° model are presented at the same cowl position and Reynolds number as previously presented for the 30° model.) Figures 17(a)–(d) demonstrate the sidewall effects of contraction ratio on the static pressures on the baseplate centerline, the sidewall centerline, and the sidewall at $y/H = 0.87$ and $y/H = 0.13$, respectively. Figure 17(a) reveals that the effect of increasing contraction ratio yields an overall upward shift in the pressure distribution. As with the 30° data, the baseplate boundary layer and its associated weak leading-edge shock isolate the centerline of the baseplate from the sharp pressure peaks where the sidewall shocks intersect at the centerline. Figure 17(b) presents the sidewall centerline pressure distribution. The 30° data indicated that as the contraction ratio was increased, the incident shock location moved forward; there was also an increase in compression. The location of the instrumentation on the 70° model did not provide sufficient resolution to indicate any shift in impingement location. Because the modified oblique shock theory predicted sidewall shock impingements in the region of $x'/T'_x = 0.47$ to 0.63 (followed by shock detachment), and because only one orifice was located in that region, the pressure rise caused by the impingement and the location of the impingement are not resolved. For each of the contraction ratios, the highest measured pressure was immediately ahead of the shoulder at the beginning of the throat ($x'/T'_x = 0.994$) on the sidewall centerline. The configuration with $CR = 3$ is the only configuration for which the pressure decreases and then rises again as if there were an expansion followed by a shock impingement. At the higher contraction ratios, these interactions are closer together, because the closer sidewalls decrease the distance between shock reflections. Because the modified oblique shock theory predicted detached shocks upstream of the throat, it is unlikely that this reflecting shock model describes the flow field. For the contraction ratios of 5 and 9, the pressure relaxes monotonically downstream of the shoulder. This pressure relaxation was also evident in the

sidewall data at $y/H = 0.87$ (fig. 17(c)). The sidewall at $y/H = 0.13$ (fig. 17(d)) indicates that the axial pressure increase upstream of the throat intensifies with increasing contraction ratio, which could be a result of the more forward placement of the glancing shocks with increased contraction ratio.

Leading-edge sweep effects. Figures 18(a) and (b) show the effect of leading-edge sweep on the baseplate and sidewall centerline pressure distribution, respectively, for the $CR = 3$, 0-percent cowl configuration at $N_{Re} = 5.50 \times 10^5$ per foot. Modified oblique shock theory predicts that the compression across the leading-edge shock will increase by approximately 4 percent when Λ is increased from 30° to 70°. After the flow passes through two shocks, this margin increases to 13 percent. These data indicate, however, that the compression for the $\Lambda = 70^\circ$ configuration is significantly less than for the 30° configuration. The importance of flow spillage on internal pressure relief is illustrated by the fact that the spillage yields a pressure relief sufficient to overcome the increase that was predicted inviscidly (neglecting end effects) on both the sidewall and the baseplate.

Reynolds number variation. Reynolds number effects were studied for $CR = 3$, 0-percent cowl configuration with $\Lambda = 30^\circ$ (figs. 19(a) and (b)) and $\Lambda = 70^\circ$ (figs. 20(a) and (b)). Decreasing the Reynolds number causes the viscous forces to take on greater significance with respect to the momentum forces. Hence, boundary-layer thickness is expected to increase; of more importance to the inviscid flow field is the fact that the displacement thickness increases and causes all surfaces to possess effectively larger wedge angles. This in turn generates stronger shocks and increases the internal compression of the inlet. Figures 19(a) and (b) present baseplate and sidewall centerline pressure distributions for a configuration with a 30° leading-edge sweep, a 0-percent cowl, and a contraction ratio of 3 at free-stream Reynolds numbers of 0.89×10^5 , 2.89×10^5 , and 5.50×10^5 per foot. Although the Reynolds number range obtained in the present work spans less than an order of magnitude, the Reynolds number effect is significant; a 27-percent increment in peak pressure is observed on the baseplate centerline. Figure 19(b) shows some forward movement of the sidewall shock impingement points (due to increasing shock angles), but the instrumentation density is insufficient to quantify the extent of the shock movement.

Figures 20(a) and (b) show the pressure distributions on the baseplate and sidewall centerlines,

respectively, for the 70° leading-edge sweep configuration over the same range of Reynolds numbers. Trends similar to the 30° data are noted, but the magnitude of the increment in peak baseplate centerline pressure distribution is decreased to approximately 17 percent, compared with 27 percent for $\Lambda = 30^\circ$ (i.e., the Reynolds number effects appear to attenuate with (or be dominated by) increasing Λ). The measured decrease in pressure with increased Λ suggests weaker shocks, which do not interact as strongly with the baseplate boundary layer.

Concluding Remarks

Three-dimensional sidewall-compression scramjet inlets with leading-edge sweeps of 30° and 70° have been tested in the Langley Hypersonic CF₄ Tunnel at Mach 6 and a ratio of specific heats of 1.2 to examine the effects of leading-edge sweep, cowl position, contraction ratio, and Reynolds number on the internal flow interactions. The present work also represents the first step toward obtaining a characterization of simulated real-gas effects on inlet flow fields. Admittedly, simulation of the effects of low ratios of specific heat γ in tetrafluoromethane (CF₄) is approximate because of the variation of γ within the shock layer along or around a reentering vehicle, in contrast to the nearly constant γ within the shock layer in CF₄. However, the facility provides a lower bound for the assessment of γ effects that cannot be obtained in other ground test facilities. To obtain the explicit effects of low γ , the model must be tested in both CF₄ and air, and the present work has fulfilled the first phase of that work.

Of particular interest for the combined project are the inlet starting characteristics. It was not known prior to testing whether the model could start in a low- γ environment. More important to the wind tunnel experiment is that, because these models were the largest tested to date in the CF₄ facility, it was not known whether the tunnel would unstart (because of blockage effects) once the model was injected into the flow. Based on schlieren movies taken of each run, both the tunnel and the inlet appeared to start and remain started for each configuration tested. The schlieren movies indicated that the flow was steady on an 8-msec time scale and showed the effect of the internal flow on the external flow in terms of spillage.

To obtain an approximate characterization of the flow field, a modification of two-dimensional inviscid oblique shock theory was derived to accommodate the three-dimensional effects of leading-edge sweep. This theory qualitatively predicted the reflected shock structure (i.e., sidewall impingement

locations) and the observed increase in spillage with increasing leading-edge sweep.

Two generalizations can be made when comparing the 30° and 70° data. First, for a given contraction ratio and cowl position, the 70° sweep inlet provides generally lower compression than the 30° leading-edge sweep inlet. Second, the 70° model provides more spillage. The former is in fact a direct result of the latter. The modified oblique shock theory and the schlieren photographs indicate that increasing the sweep angle enhances the spillage. Thus, the 30° sweep inlet configuration would be expected to capture more of the high-pressure fluid and have a higher effective compression than the 70° configuration. Further, the shock sheets emanating from the 70° sidewalls are more inclined, and hence more susceptible, to shock detachment.

The primary effect of moving the cowl forward is capturing the flow that would have otherwise spilled ahead of the cowl. Large pressures on the cowl result from the shock formed on the cowl leading edge when the flow that was deflected by the swept sidewall leading edges impacts the free-stream aligned cowl. When the cowl is in the aft position, this deflected flow simply spills out ahead of the cowl. Sidewall and baseplate pressures indicate that the effect of the cowl position on internal pressures is limited to the immediate vicinity of the cowl.

For both the 30° and 70° leading-edge sweep angles, increased contraction ratio increases the pressure distribution throughout the inlet. With the sidewalls closer together, the leading-edge shock sheet encounters the centerline farther forward and hence reflects more times prior to reaching the throat. Each of these reflected oblique shocks incrementally increases the pressure. Although the Reynolds number range obtained in the present work spanned less than an order of magnitude, an overall increase in inlet compression (the magnitude of which decreased with increasing leading-edge sweep angle) was noted with decreasing Reynolds number. The instrumentation density was insufficient to resolve the accompanying forward shift in sidewall shock impingement location. The modified oblique shock theory provides general information on the salient features of the shock structure. In particular, the location of the first incident shock is adequately identified and the trends associated with flow spillage are given.

The present work has therefore provided an inviscid model of the internal shock structure of three-dimensional inlets, has added to a sparse data base of inlet tests in complex gases (first known inlet

test in CF_4), and has made a first step toward the explicit attainment of low- γ effects. To more fully document the flow field, particularly the 70° configuration, where a centerline Mach number reflection is likely, a more heavily instrumented model in con-

junction with a full three-dimensional Navier-Stokes computational fluid dynamics solution is required.

NASA Langley Research Center
Hampton, VA 23681-0001
September 23, 1993

Appendix

Only slight modifications to inviscid two-dimensional (2-D) oblique shock theory are required to allow for the inclusion of leading-edge sweep. The equations are presented here for a perfect gas. The extension to a viral gas such as CF_4 requires an iterative calculation of the shock angles and properties with the appropriate gas model.

Figure 21 shows the oncoming free-stream Mach vector broken into components parallel and normal to the swept leading edge. Two-dimensional oblique shock theory may be applied directly to the normal component M_{1n} to determine its postshock components; the effective sidewall-compression angle, the wedge angle measured normal to the leading edge, is given by

$$\delta_{\text{eff}} = \tan^{-1} \left(\frac{\tan \delta}{\cos \Lambda} \right) \quad (1)$$

and is greater than δ . The perfect gas equations to find the resultant Mach vector behind the oblique shock for the 2-D theory may be found in several references (e.g., ref. 27) where three equations can be combined to give (in the notation of this study) M_{2n} in terms of M_{1n} , the ratio of specific heats, and the effective wedge and shock angles as

$$M_{2n} = \frac{\left\{ \frac{M_{1n}^2 \sin^2 \theta_{\text{eff}} + \left[\frac{2}{\gamma-1} \right] \right\}^{1/2}}{\left[\frac{2\gamma}{\gamma-1} \right] M_{1n}^2 \sin^2 \theta_{\text{eff}} - 1} \sin(\theta_{\text{eff}} - \delta_{\text{eff}}) \quad (2)$$

The parallel (or crossflow) component M_{1p} must be treated separately. Although the component of velocity parallel to the shock remains unchanged through the shock, the Mach number associated with that velocity vector decreases as a result of the increase in static temperature and hence the speed of sound across the shock, as

$$M_{2p} = M_{1p} \left(\frac{T_1}{T_2} \right)^{1/2} = M_1 \sin \Lambda \left(\frac{T_1}{T_2} \right)^{1/2} \quad (3)$$

When the components behind the shock are known, the resultant magnitude and direction of the Mach vector can be determined. The spillage angle ζ is defined as the difference between two angles, Γ and β , in the plane of the wedge, as shown in figure 21. The angle the leading edge makes with the x - z plane measured in the plane of the wedge is given by

$$\Gamma = \sin^{-1} \left(\frac{\sin \delta}{\sin \delta_{\text{eff}}} \right) \quad (4)$$

The angle that the resultant makes with the leading edge in the plane of the wedge is given by

$$\beta = \tan^{-1} \left(\frac{M_{2n}}{M_{2p}} \right) = \tan^{-1} \left[\frac{M_{2n}}{(T_1/T_2)^{1/2} M_1 \sin \Lambda} \right] \quad (5)$$

The spillage angle is the difference between these two angles as follows:

$$\begin{aligned} \zeta &= \Gamma - \beta \\ &= \sin^{-1} \left(\frac{\sin \delta}{\sin \delta_{\text{eff}}} \right) - \tan^{-1} \left[\frac{M_{2n}}{(T_1/T_2)^{1/2} M_1 \sin \Lambda} \right] \end{aligned} \quad (6)$$

An alternate but equivalent definition of the spillage angle is the difference between the angle made by the resultant M_2 and its component normal to the leading edge M_{2n} and the angle between the x - y plane and M_{2n} ; both angles are measured in the plane of the wedge (see fig. 4). This alternate equation may be more convenient for some applications and is hence provided for reference as follows:

$$\zeta = \tan^{-1} \left(\frac{M_{2p}}{M_{2n}} \right) - \tan^{-1} (\cos \delta_{\text{eff}} \tan \Lambda) \quad (7)$$

For all the cases considered in the present work, the spillage is on the order of a couple of degrees. Once the conditions behind the first shock are computed, the process is repeated for each shock upstream of the cowl leading edge. Performance quantities (e.g., total pressure recovery, η_{ke} , etc.) and the mass capture (based on total spillage) can then be computed.

References

- Williams, Robert M.: National Aero-Space Plane: Technology for America's Future. *Aerosp. America*, vol. 24, no. 11, Nov. 1986, pp. 18-22.
- Kandebo, Stanley W.: Researchers Pursue X-30 Spaceplane Technologies for 1990 Evaluation. *Aviation Week & Space Technol.*, vol. 129, no. 6, Aug. 8, 1988, pp. 49, 53.
- Henry, John R.; and Anderson, Griffin Y.: *Design Considerations for the Airframe Integrated Scramjet*. NASA TM X-2895, 1973.
- Kumar, Ajay; Singh, D. J.; and Trexler, Carl A.: Numerical Study of the Effects of Reverse Sweep on Scramjet Inlet Performance. *J. Propuls. & Power*, vol. 8, no. 3, May-June 1992, pp. 714-719.
- Holland, Scott D.; and Perkins, John N.: Internal Shock Interactions in Propulsion/Airframe Integrated Three-Dimensional Sidewall Compression Scramjet Inlets. AIAA-92-3099, July 1992.
- Jones, Robert A.; and Hunt, James L. (appendix A by James L. Hunt, Kathryn A. Smith, and Robert B. Reynolds and appendix B by James L. Hunt and Lillian R. Boney): *Use of Tetrafluoromethane To Simulate Real-Gas Effects on the Hypersonic Aerodynamics of Blunt Vehicles*. NASA TR R-312, 1969.
- Miller, Charles G., III: *Measured Pressure Distributions, Aerodynamic Coefficients, and Shock Shapes on Blunt Bodies at Incidence in Hypersonic Air and CF₄*. NASA TM-84489, 1982.
- Micol, John R.: Simulation of Real-Gas Effects on Pressure Distributions for a Proposed Aeroassist Flight Experiment Vehicle and Comparison to Prediction. AIAA-87-2368, Aug. 1987.
- Midden, Raymond E.; and Miller, Charles G., III: *Description and Calibration of the Langley Hypersonic CF₄ Tunnel—A Facility for Simulating Low γ Flow as Occurs for a Real Gas*. NASA TP-2384, 1985.
- Holland, Scott D.: *Schlieren Photographs and Internal Pressure Distributions for Three-Dimensional Sidewall-Compression Scramjet Inlets at a Mach Number of 6 in CF₄*. NASA TM-4479, 1993.
- Northam, G. Burton; and Anderson, Griffin Y.: Survey of Supersonic Combustion Ramjet Research at Langley. AIAA-86-0159, Jan. 1986.
- Trexler, Carl A.: Performance of an Inlet for an Integrated Scramjet Concept. *J. Aircr.*, vol. 11, no. 9, Sept. 1974, pp. 589-591.
- Trexler, Carl A.: Inlet Performance of the Integrated Langley Scramjet Module (Mach 2.3 to 7.6). AIAA-75-1212, Sept.-Oct. 1975.
- Trexler, Carl A.; and Souders, Sue W.: *Design and Performance at a Local Mach Number of 6 of an Inlet for an Integrated Scramjet Concept*. NASA TN D-7944, 1975.
- Trexler, Carl A.: Inlet Starting Predictions for Sidewall-Compression Scramjet Inlets. AIAA-88-3257, July 1988.
- Trexler, Carl A.: *Tests of Two Sidewall-Compression Scramjet Inlets at Mach 18.1 to 21.6 in Helium*. NASP TM-1018, 1988.
- Micol, John R.; Midden, Raymond E.; and Miller, Charles G., III: Langley 20-Inch Hypersonic CF₄ Tunnel: A Facility for Simulating Real-Gas Effects. AIAA-92-3939, July 1992.
- Sutton, Kenneth: *Relations for the Thermodynamic and Transport Properties in the Testing Environment of the Langley Hypersonic CF₄ Tunnel*. NASA TM-83220, 1981.
- Chari, Nallan Chakravartula Satyanarayana: *Thermodynamic Properties of Carbon Tetrafluoride*. Ph.D. Thesis, Univ. of Mich., 1960.
- Hunt, James L.; and Boney, Lillian R.: *Thermodynamic and Transport Properties of Gaseous Tetrafluoromethane in Chemical Equilibrium*. NASA TN D-7181, 1973.
- Talcott, Noel A., Jr.: *Thermodynamic Properties of Gaseous Fluorocarbons and Isentropic Equilibrium Expansions of Two Binary Mixtures of Fluorocarbons and Argon*. NASA TN D-8405, 1977.
- Kumar, Ajay: Three-Dimensional Inviscid Analysis of the Scramjet Inlet Flow Field. AIAA-82-0060, Jan. 1982.
- Kutschenreuter, Paul H., Jr.; Keith, James S.; Weil, James A.; and Nettleton, Paul H.: *Investigation of Hypersonic Inlet Shock-Wave Boundary Layer Interaction*. AFFDL-TR-65-36, U.S. Air Force, Mar. 1965. (Available from DTIC as AD 464 057.)
- Settles, G. S.; and Dolling, D. S.: Swept Shock/Boundary-Layer Interactions Tutorial and Update. AIAA-90-0375, Jan. 1990.
- Garrison, T. J.; Settles, G. S.; Narayanswami, N.; and Knight, D. D.: Structure of Crossing-Shock Wave/Turbulent Boundary-Layer Interactions. AIAA-92-3670, July 1992.
- Holland, Scott D.: A Computational and Experimental Investigation of a Three-Dimensional Hypersonic Scramjet Inlet Flow Field. Ph.D. Diss., North Carolina State Univ., 1991.
- Anderson, John D., Jr.: *Modern Compressible Flow—With Historical Perspective*. McGraw-Hill, Inc., c.1982.

Table 1. Test Matrix for $\Lambda = 30^\circ$ Model

Contraction ratio (CR)	Reynolds number per foot at each cowl position—		
	0 percent	25 percent	No cowl
3	0.89×10^5 2.85 5.50	5.50×10^5	5.50×10^5
5	5.50×10^5	5.50×10^5	5.50×10^5
9	5.50×10^5	5.50×10^5	5.50×10^5

Table 2. Test Matrix for $\Lambda = 70^\circ$ Model

Contraction ratio (CR)	Reynolds number per foot at each cowl position—		
	0 percent	25 percent	No cowl
3	0.89×10^5 2.85 5.50	5.50×10^5	5.50×10^5
5	5.50×10^5	5.50×10^5	5.50×10^5
9	5.50×10^5	0.89×10^5 2.85 5.50	5.50×10^5

Table 3. Free-Stream and Postnormal-Shock Flow Conditions for $N_{Re} = 0.89 \times 10^5$ Per Foot
[CF₄ Tunnel; run 2289; Time = 7 sec]

Reservoir stagnation conditions:

$p_{t,1}$, N/m ² (psia)	0.1853E+07 (0.2687E+03)
$T_{t,1}$, K (°R)	0.6317E+03 (0.1137E+04)
$\rho_{t,1}$, kg/m ³ (lbm/ft ³)	0.3083E+02 (0.1924E+01)
$Z_{t,1}$	0.1007E+01
$h_{t,1}$, J/kg (Btu/lbm)	0.6298E+06 (0.2709E+03)

Free-stream conditions (flow not saturated):

p_1 , N/m ² (psia)	0.5165E+02 (0.7491E-02)
T_1 , K (°R)	0.1623E+03 (0.2921E+03)
ρ_1 , kg/m ³ (lbm/ft ³)	0.3369E-02 (0.2103E-03)
q_1 , N/m ² (psia)	0.1245E+04 (0.1805E+00)
h_1 , J/kg (Btu/lbm)	0.2603E+06 (0.1120E+03)
u_1 , m/sec (ft/sec)	0.8596E+03 (0.2820E+04)
$N_{Re,1}$, m ⁻¹ (ft ⁻¹)	0.2912E+06 (0.8877E+05)
μ_1 , N-sec/m ² (lbm/ft-sec)	0.9945E-05 (0.6683E-05)
M_1	0.6237E+01
Z_1	0.1000E+01
γ_1	0.1239E+01
$N_{Pr,1}$	0.8511E+00

Static conditions behind normal shock:

p_2 , N/m ² (psia)	0.2328E+04 (0.3376E+00)
T_2 , K (°R)	0.6275E+03 (0.1129E+04)
ρ_2 , kg/m ³ (lbm/ft ³)	0.3926E-01 (0.2451E-02)
u_2 , m/sec (ft/sec)	0.7376E+02 (0.2420E+03)
h_2 , J/kg (Btu/lbm)	0.6270E+06 (0.2697E+03)
$N_{Re,2}$, m ⁻¹ (ft ⁻¹)	0.9370E+05 (0.2856E+05)
Z_2	0.1000E+01
M_2	0.2881E+00
γ_2	0.1106E+01
$N_{Pr,2}$	0.7574E+00

Stagnation conditions behind normal shock:

$p_{t,2}$, N/m ² (psia)	0.2437E+04 (0.3534E+00)
$T_{t,2}$, K (°R)	0.6302E+03 (0.1134E+04)
$\rho_{t,2}$, kg/m ³ (lbm/ft ³)	0.4092E-01 (0.2555E-02)
$Z_{t,2}$	0.1000E+01
$h_{t,2}$, J/kg (Btu/lbm)	0.6297E+06 (0.2709E+03)
$\gamma_{t,2}$	0.1106E+01

Table 4. Free-Stream and Postnormal-Shock Flow Conditions for $N_{Re} = 2.85 \times 10^5$ Per Foot
[CF₄ Tunnel; run 2290; Time = 7 sec]

Reservoir stagnation conditions:

$p_{t,1}$, N/m ² (psia)	0.6607E+07 (0.9583E+03)
$T_{t,1}$, K (°R)	0.6511E+03 (0.1172E+04)
$\rho_{t,1}$, kg/m ³ (lbm/ft ³)	0.1042E+03 (0.6504E+01)
$Z_{t,1}$	0.1031E+01
$h_{t,1}$, J/kg (Btu/lbm)	0.6462E+06 (0.2780E+03)

Free-stream conditions (flow not saturated):

p_1 , N/m ² (psia)	0.1761E+03 (0.2555E-01)
T_1 , K (°R)	0.1688E+03 (0.3038E+03)
ρ_1 , kg/m ³ (lbm/ft ³)	0.1105E-01 (0.6897E-03)
q_1 , N/m ² (psia)	0.4228E+04 (0.6132E+00)
h_1 , J/kg (Btu/lbm)	0.2636E+06 (0.1134E+03)
u_1 , m/sec (ft/sec)	0.8749E+03 (0.2870E+04)
$N_{Re,1}$, m ⁻¹ (ft ⁻¹)	0.9348E+06 (0.2849E+06)
μ_1 , N-sec/m ² (lbm/ft-sec)	0.1034E-04 (0.6948E-05)
M_1	0.6240E+01
Z_1	0.1000E+01
γ_1	0.1233E+01
$N_{Pr,1}$	0.8330E+00

Static conditions behind normal shock:

p_2 , N/m ² (psia)	0.7914E+04 (0.1148E+01)
T_2 , K (°R)	0.6441E+03 (0.1159E+04)
ρ_2 , kg/m ³ (lbm/ft ³)	0.1300E+00 (0.8119E-02)
u_2 , m/sec (ft/sec)	0.7432E+02 (0.2438E+03)
h_2 , J/kg (Btu/lbm)	0.6435E+06 (0.2768E+03)
$N_{Re,2}$, m ⁻¹ (ft ⁻¹)	0.3070E+06 (0.9357E+05)
Z_2	0.1000E+01
M_2	0.2866E+00
γ_2	0.1105E+01
$N_{Pr,2}$	0.7541E+00

Stagnation conditions behind normal shock:

$p_{t,2}$, N/m ² (psia)	0.8280E+04 (0.1201E+01)
$T_{t,2}$, K (°R)	0.6469E+03 (0.1164E+04)
$\rho_{t,2}$, kg/m ³ (lbm/ft ³)	0.1355E+00 (0.8458E-02)
$Z_{t,2}$	0.1000E+01
$h_{t,2}$, J/kg (Btu/lbm)	0.6462E+06 (0.2780E+03)
$\gamma_{t,2}$	0.1105E+01

Table 5. Free-Stream and Postnormal-Shock Flow Conditions for $N_{Re} = 5.50 \times 10^5$ Per Foot
[CF₄ Tunnel; run 2284; Time = 7 sec]

Reservoir stagnation conditions:

$p_{t,1}$, N/m ² (psia)	0.1380E+08 (0.2002E+04)
$T_{t,1}$, K (°R)	0.6711E+03 (0.1208E+04)
$\rho_{t,1}$, kg/m ³ (lbm/ft ³)	0.2023E+03 (0.1263E+02)
$Z_{t,1}$	0.1076E+01
$h_{t,1}$, J/kg (Btu/lbm)	0.6634E+06 (0.2854E+03)

Free-stream conditions (flow not saturated):

p_1 , N/m ² (psia)	0.3630E+03 (0.5265E-01)
T_1 , K (°R)	0.1760E+03 (0.3168E+03)
ρ_1 , kg/m ³ (lbm/ft ³)	0.2184E-01 (0.1363E-02)
q_1 , N/m ² (psia)	0.8652E+04 (0.1255E+01)
h_1 , J/kg (Btu/lbm)	0.2672E+06 (0.1150E+03)
u_1 , m/sec (ft/sec)	0.8902E+03 (0.2921E+04)
$N_{Re,1}$, m ⁻¹ (ft ⁻¹)	0.1804E+07 (0.5499E+06)
μ_1 , N-sec/m ² (lbm/ft-sec)	0.1077E-04 (0.7240E-05)
M_1	0.6233E+01
Z_1	0.9999E+00
γ_1	0.1227E+01
$N_{Pr,1}$	0.8170E+00

Static conditions behind normal shock:

p_2 , N/m ² (psia)	0.1621E+05 (0.2351E+01)
T_2 , K (°R)	0.6613E+03 (0.1190E+04)
ρ_2 , kg/m ³ (lbm/ft ³)	0.2595E+00 (0.1620E-01)
u_2 , m/sec (ft/sec)	0.7492E+02 (0.2458E+03)
h_2 , J/kg (Btu/lbm)	0.6606E+06 (0.2842E+03)
$N_{Re,2}$, m ⁻¹ (ft ⁻¹)	0.6062E+06 (0.1848E+06)
Z_2	0.1000E+01
M_2	0.2852E+00
γ_2	0.1104E+01
$N_{Pr,2}$	0.7507E+00

Stagnation conditions behind normal shock:

$p_{t,2}$, N/m ² (psia)	0.1695E+05 (0.2459E+01)
$T_{t,2}$, K (°R)	0.6641E+03 (0.1195E+04)
$\rho_{t,2}$, kg/m ³ (lbm/ft ³)	0.2702E+00 (0.1687E-01)
$Z_{t,2}$	0.1000E+01
$h_{t,2}$, J/kg (Btu/lbm)	0.6634E+06 (0.2854E+03)
$\gamma_{t,2}$	0.1104E+01

Table 6. Listing of Tunnel Runs

Run	CR			Cowl position			Reynolds number per foot		
	3	5	9	0%	25%	No	5.50×10^5	2.85×10^5	0.89×10^5
$\Lambda = 30^\circ$ model									
2262	x			x			x		
2263	x					x		x	
2264	x					x	x		
2265	x			x					x
2266	x			x				x	
2267	x				x		x		
2268		x			x		x		
^a 2270		x		x			x		
2271		x				x	x		
2272			x	x			x		
2273			x		x		x		
2274			x			x	x		
$\Lambda = 70^\circ$ model									
2275	x			x					x
2276	x			x				x	
2277	x			x			x		
2278	x				x		x		
2279	x					x	x		
2280	x				x		x		
2281	x			x			x		
^a 2282		x		x			x		
2284		x			x		x		
2285		x				x	x		
2286			x			x	x		
2287			x	x			x		
2288			x		x		x		
2289			x		x				x
2290			x		x			x	

^aSchlieren photograph included in this report.Table 7. Shock Impingement Locations Based on Inviscid Prediction for CF₄

CR	Centerline		Sidewall		Centerline		Sidewall		Centerline		Sidewall	
	x'/T'_x	x , in.	x'/T'_x	x , in.	x'/T'_x	x , in.	x'/T'_x	x , in.	x'/T'_x	x , in.	x'/T'_x	x , in.
$\Lambda = 30^\circ$												
3	0.67	3.36	0.91	4.59	1.14	5.75						
5	.55	2.79	.76	3.83	.95	4.79	1.03	5.19				
9	.50	2.52	.68	3.43	.86	4.34	.93	4.64	0.997	5.03	1.03	5.19
$\Lambda = 70^\circ$												
3	0.49	2.47	0.63	3.18	Detached							
5	.41	2.07	.53	2.67	Detached							
9	.37	1.87	.47	2.37	Detached							

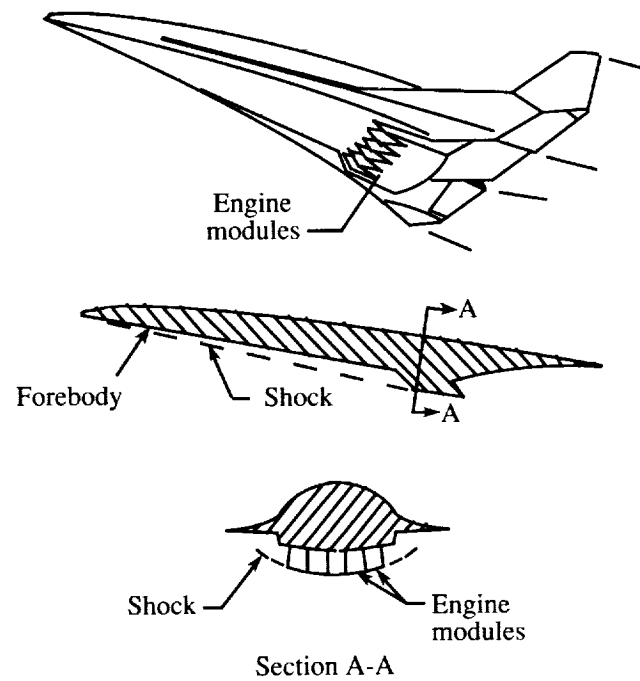


Figure 1. Propulsion airframe integration.

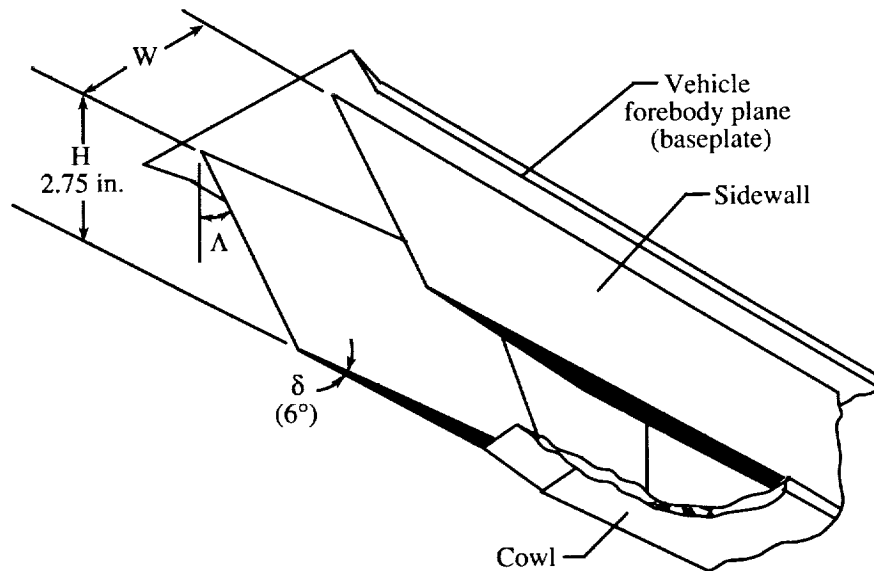
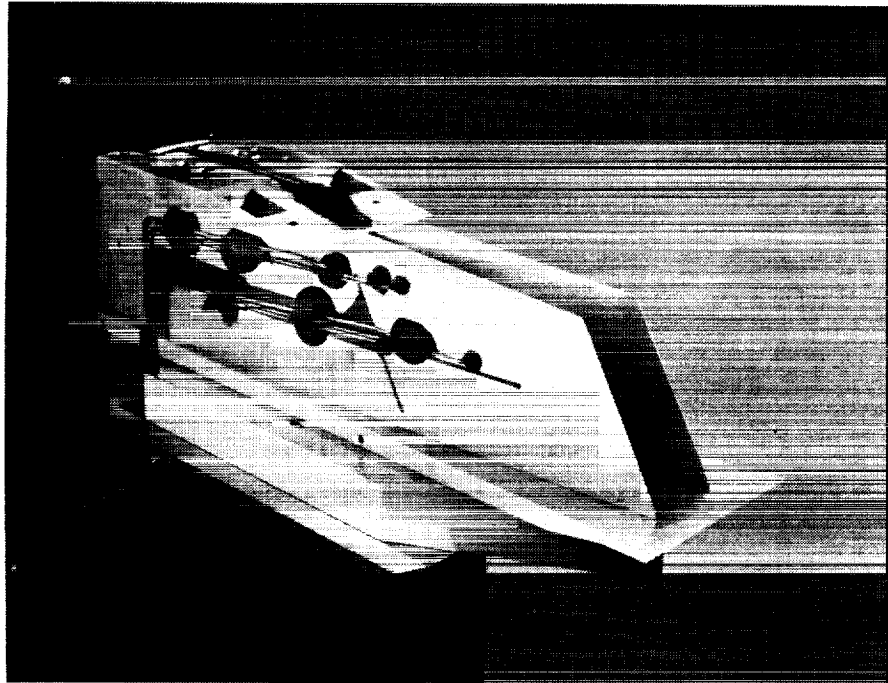


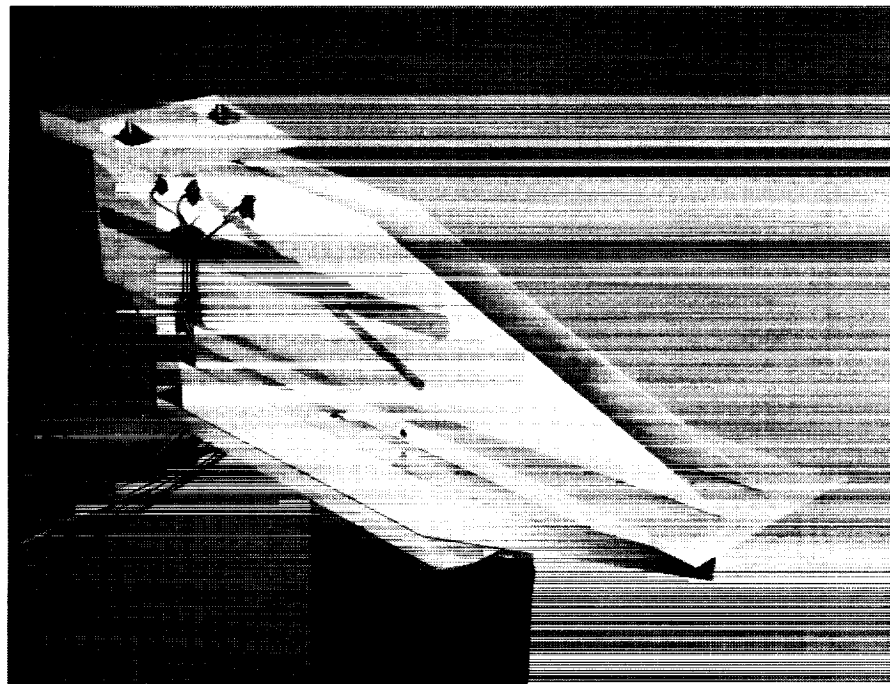
Figure 2. Modular engine construction for airframe integrated scramjet inlet (inlet shown in flight orientation).

ORIGINAL PAGE
BLACK AND WHITE PHOTOGRAPH



L-92-1782

(a) 30° inlet model.



L-92-1781

(b) 70° inlet model.

Figure 3. Generic scramjet inlet models.

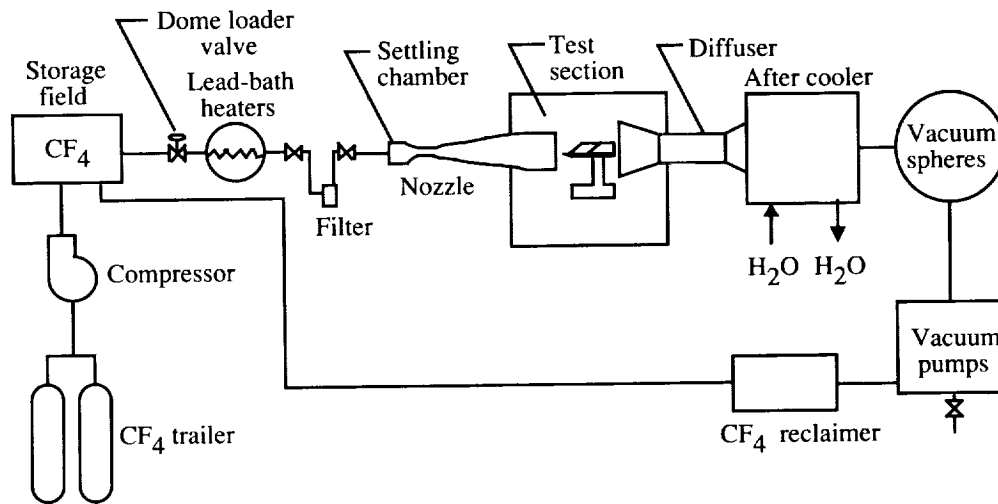


Figure 5. Schematic of Langley Hypersonic CF₄ Tunnel.

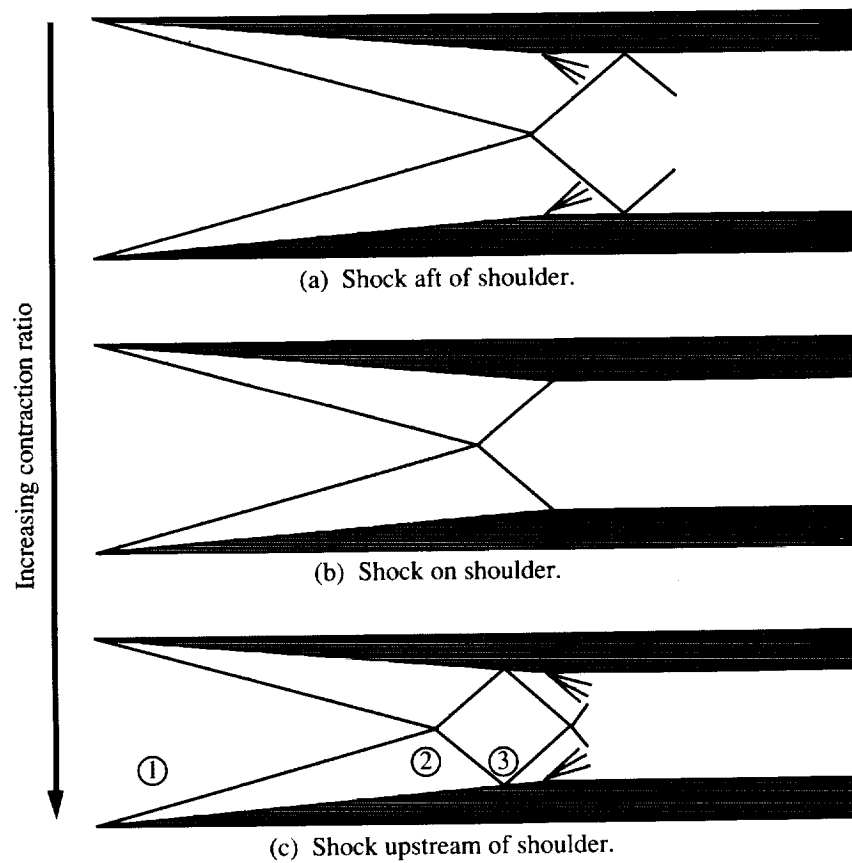


Figure 6. Inviscid shock interactions between wedges when end effects are neglected.

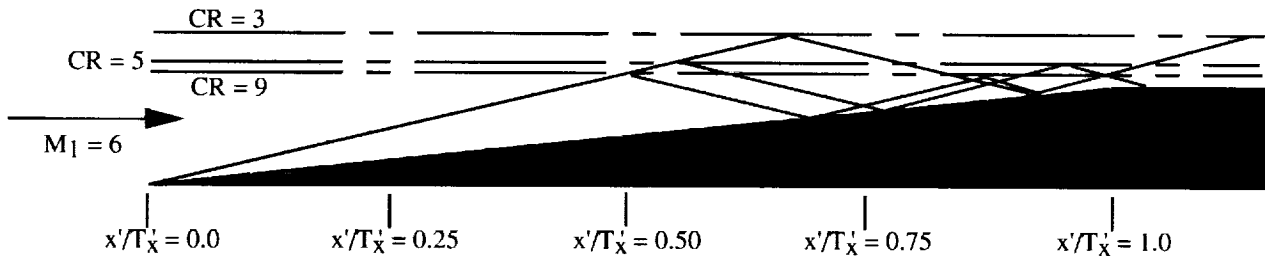


Figure 7. Scale drawing of inviscid shock location predictions for $\Lambda = 30^\circ$ configuration for contraction ratios of 3, 5, and 9.

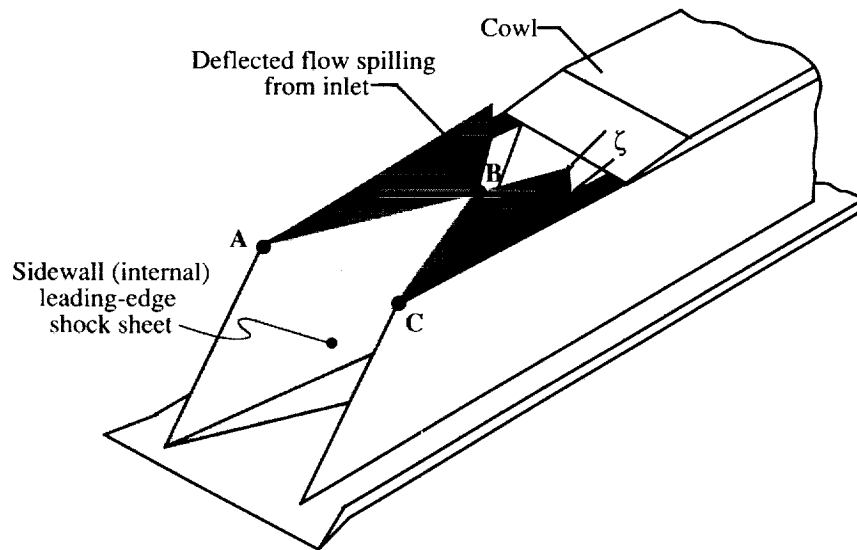


Figure 8. Region of flow deflected by internal leading-edge shock. (Additional spillage from reflected shocks not shown; spillage angle ζ exaggerated.)

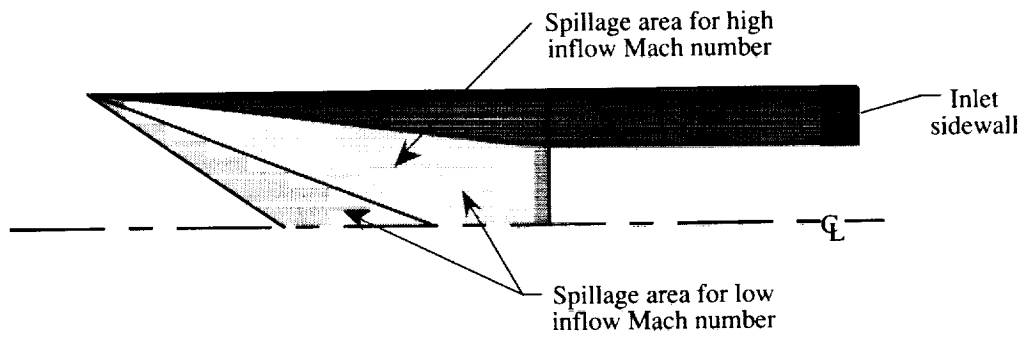


Figure 9. Effect of increased inflow Mach number on size of spillage window (region of flow deflection) in cowl plane.

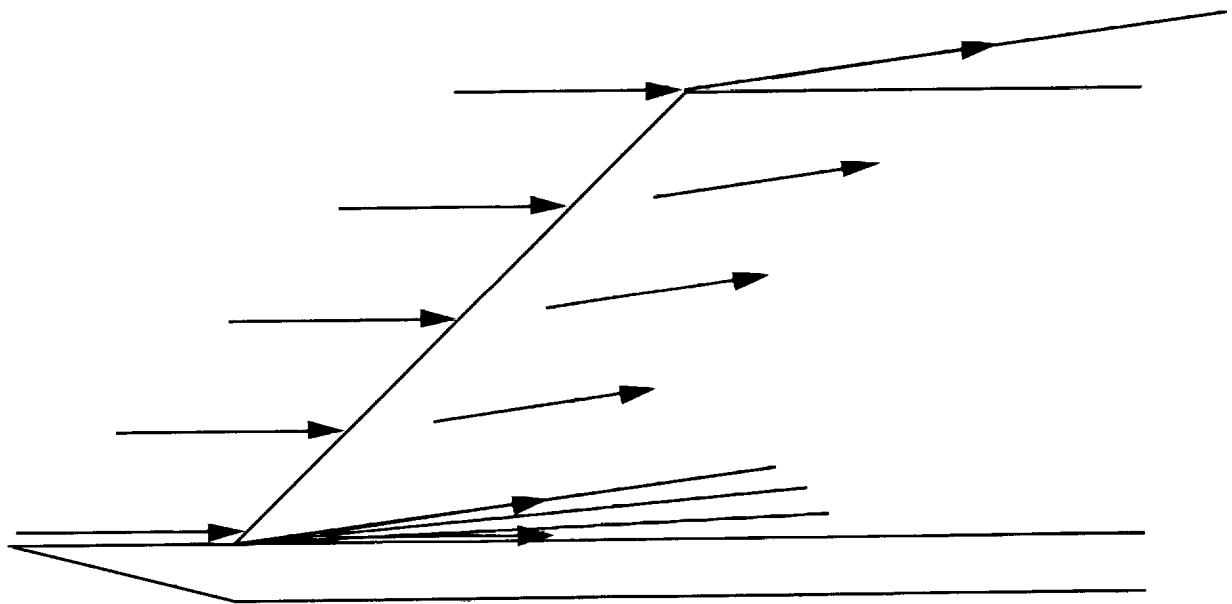
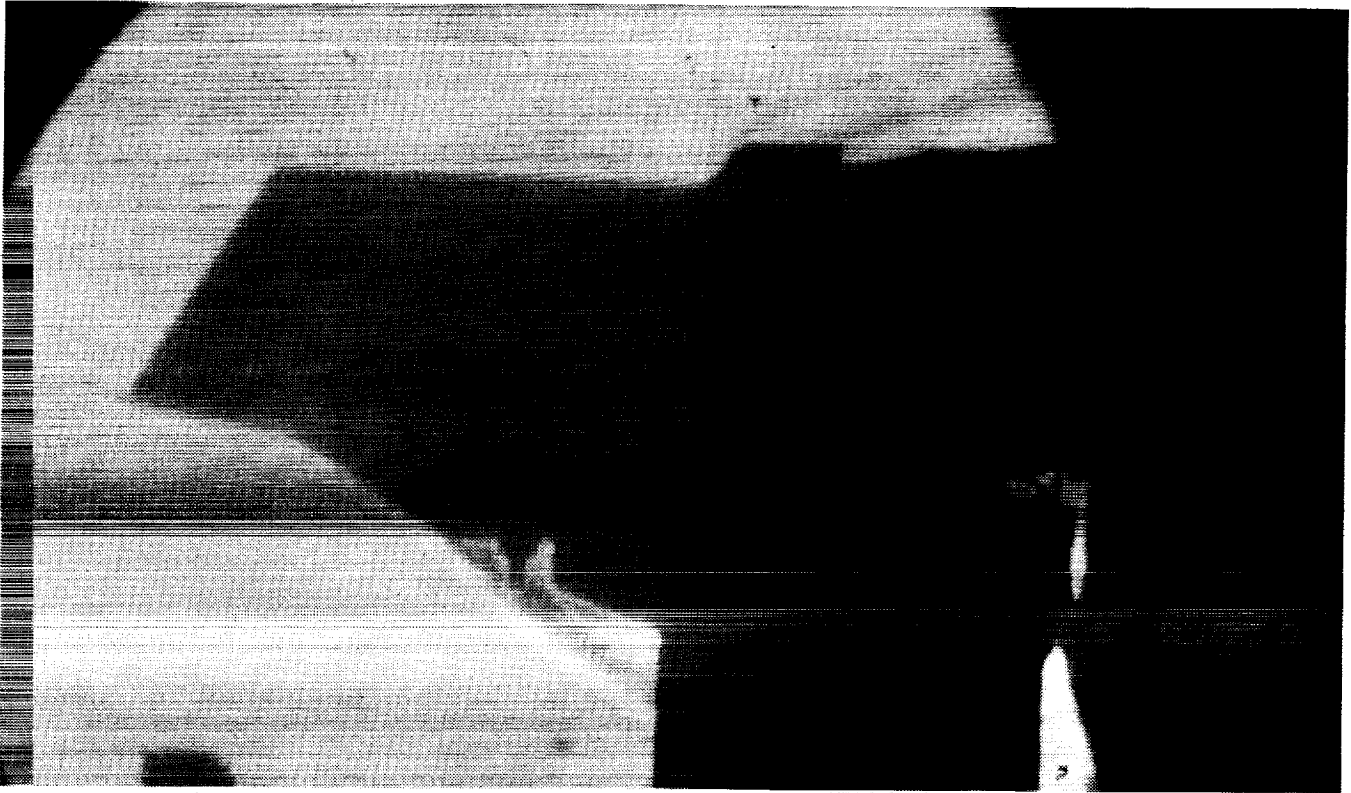


Figure 10. Centered expansion model of baseplate interaction region.

ORIGINAL PAGE
BLACK AND WHITE PHOTOGRAPH

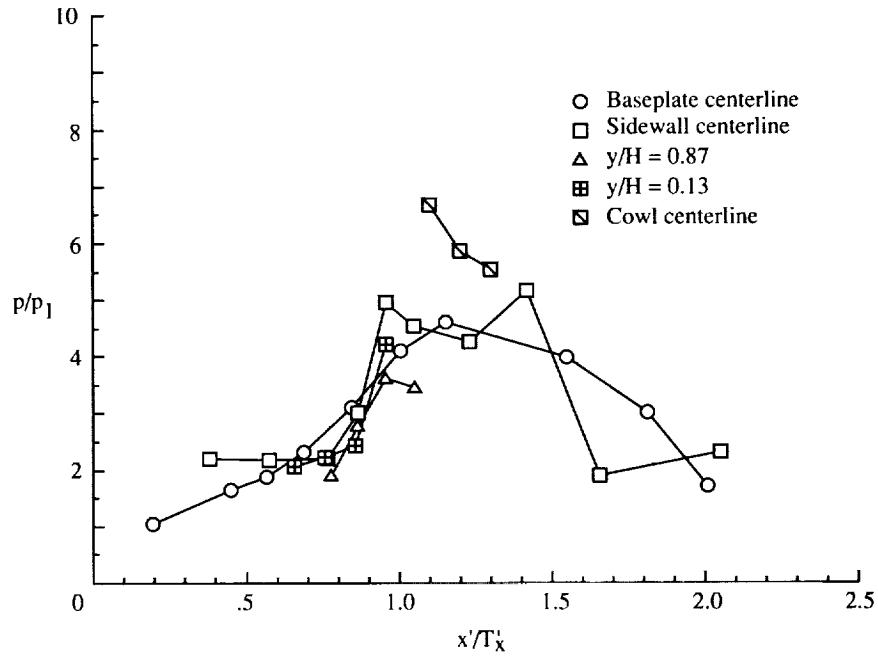


(a) Run 2270; $\Lambda = 30^\circ$.

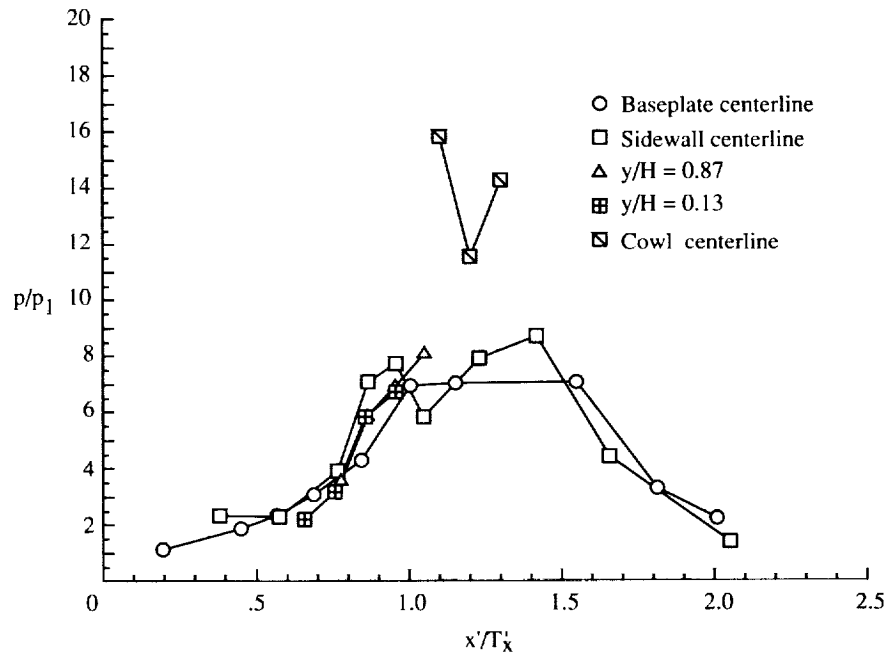


(b) Run 2282; $\Lambda = 70^\circ$.

Figure 11. Schlieren photographs of external inlet flow field. CR = 5; 0-percent cowl; $N_{Re} = 5.50 \times 10^5$ per foot.

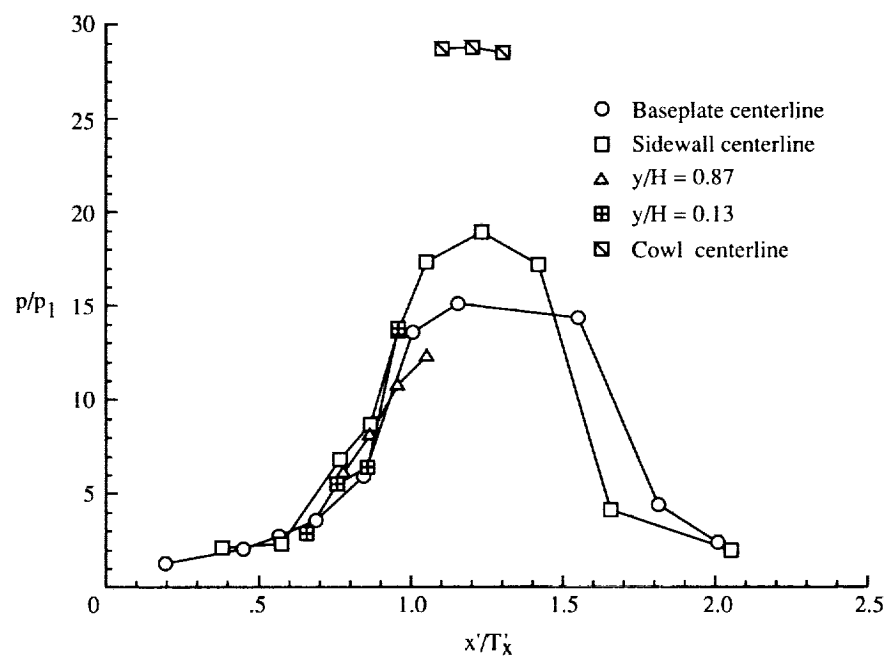


(a) Run 2262; CR = 3.



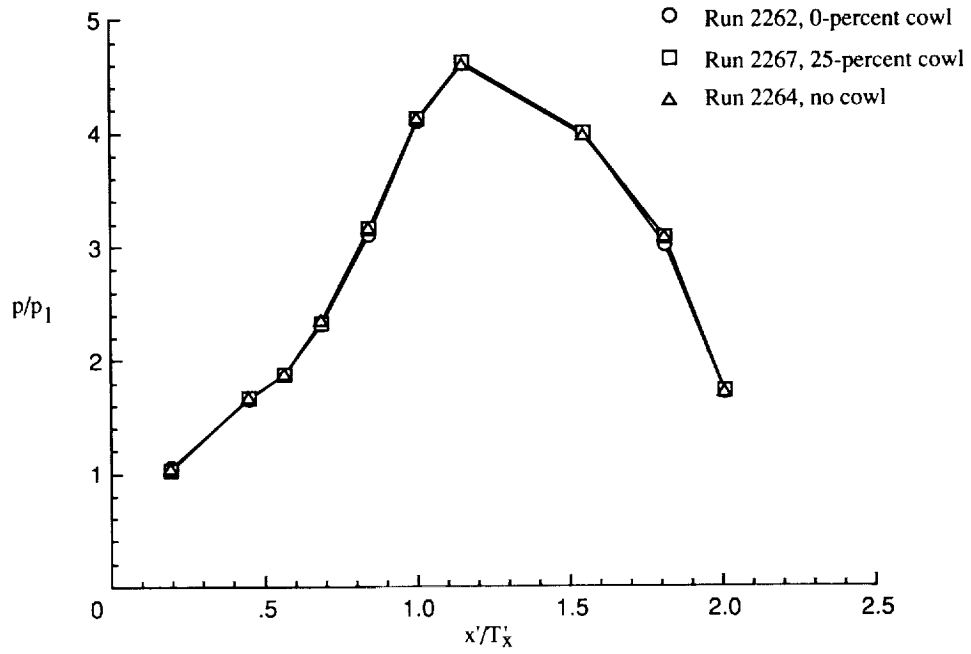
(b) Run 2270; CR = 5.

Figure 12. Configuration complete plots for $\Lambda = 30^\circ$, 0-percent cowl, and $N_{Re} = 5.5 \times 10^5$ per foot.

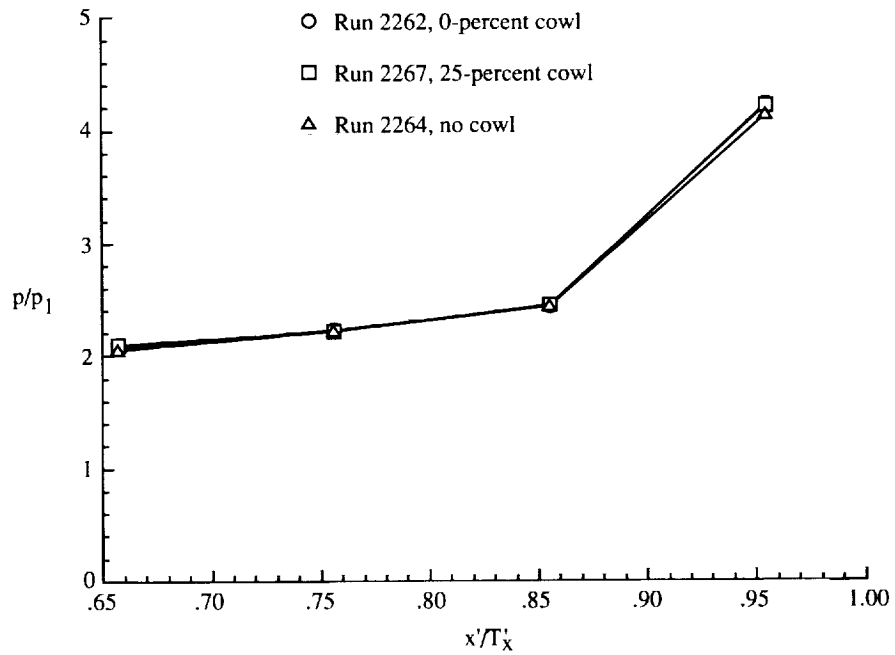


(c) Run 2272; $CR = 9$.

Figure 12. Concluded.

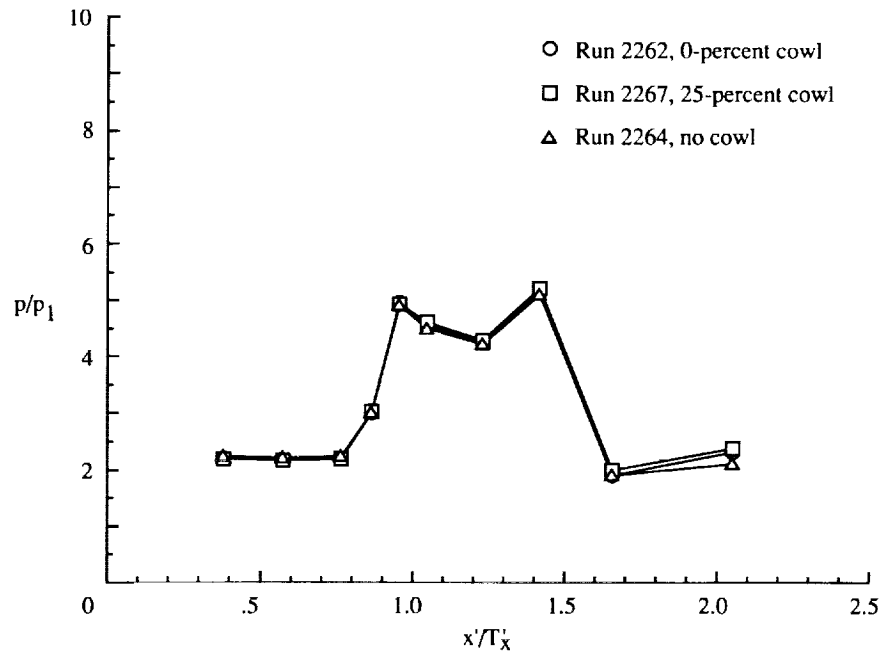


(a) Baseplate centerline.

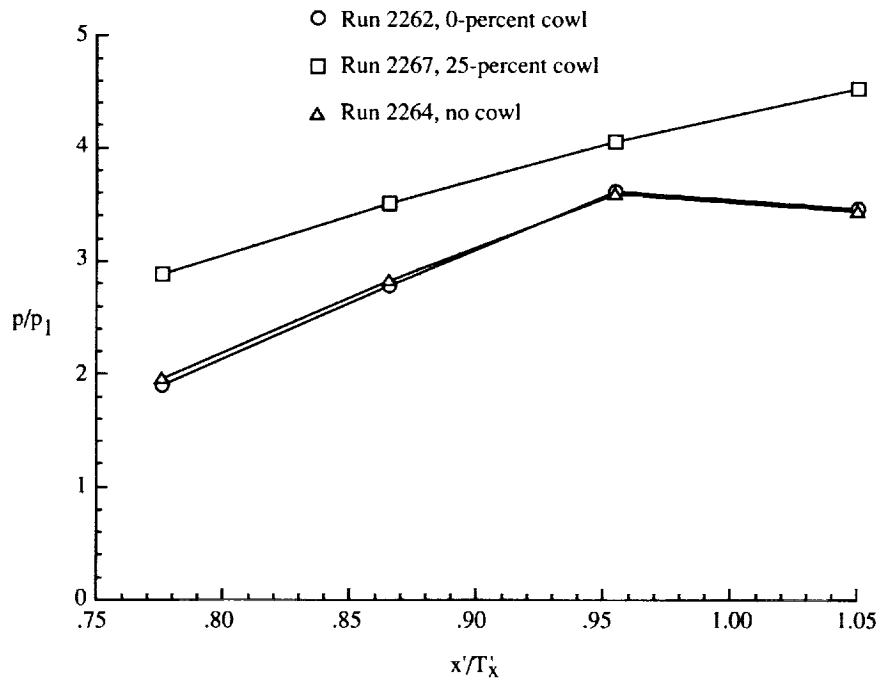


(b) Sidewall at $y/H = 0.13$.

Figure 13. Cowl effects on pressure distribution. $\Lambda = 30^\circ$; $CR = 3$; $N_{Re} = 5.50 \times 10^5$ per foot.

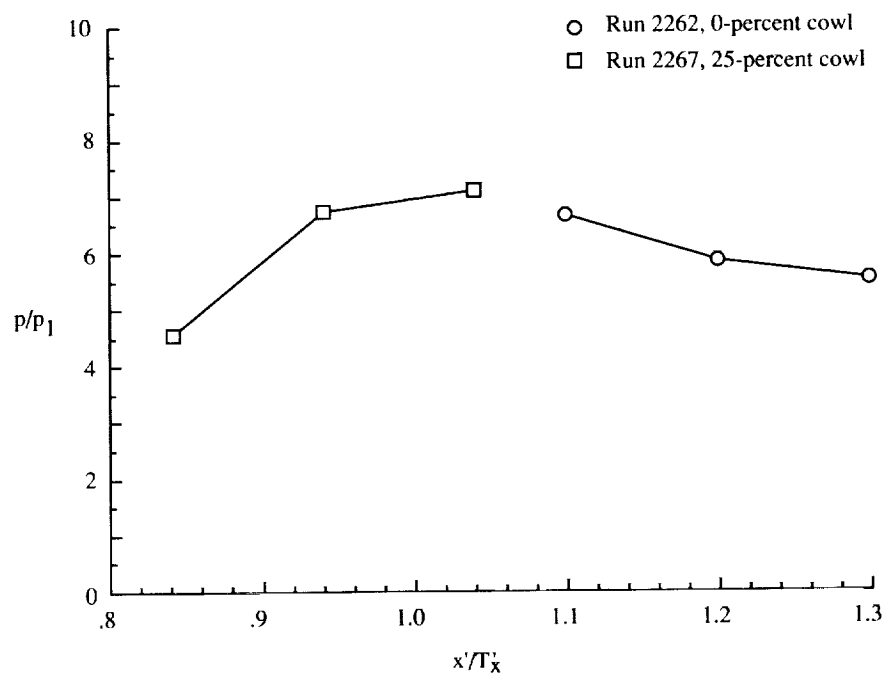


(c) Sidewall centerline.



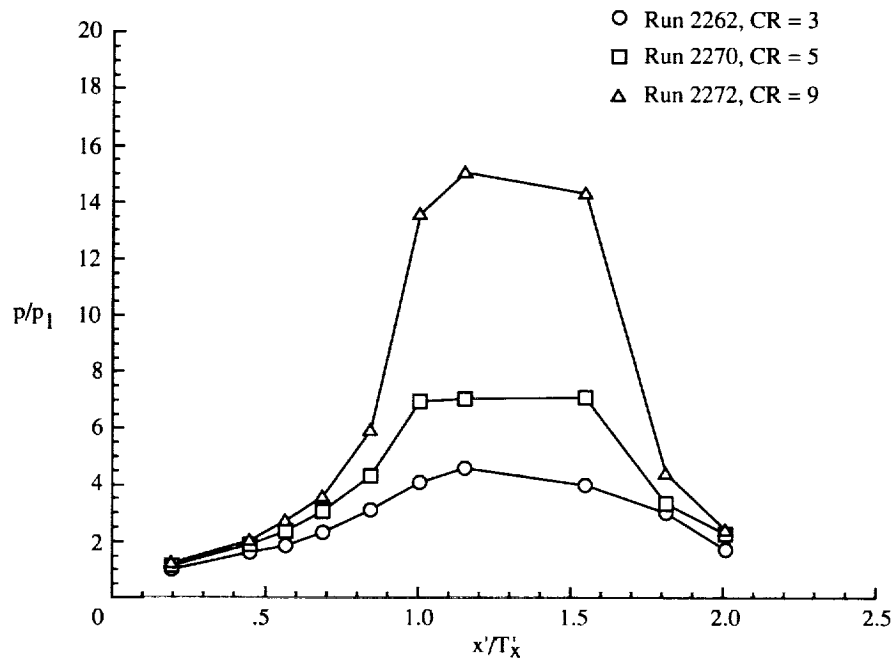
(d) Sidewall at $y/H = 0.87$.

Figure 13. Continued.

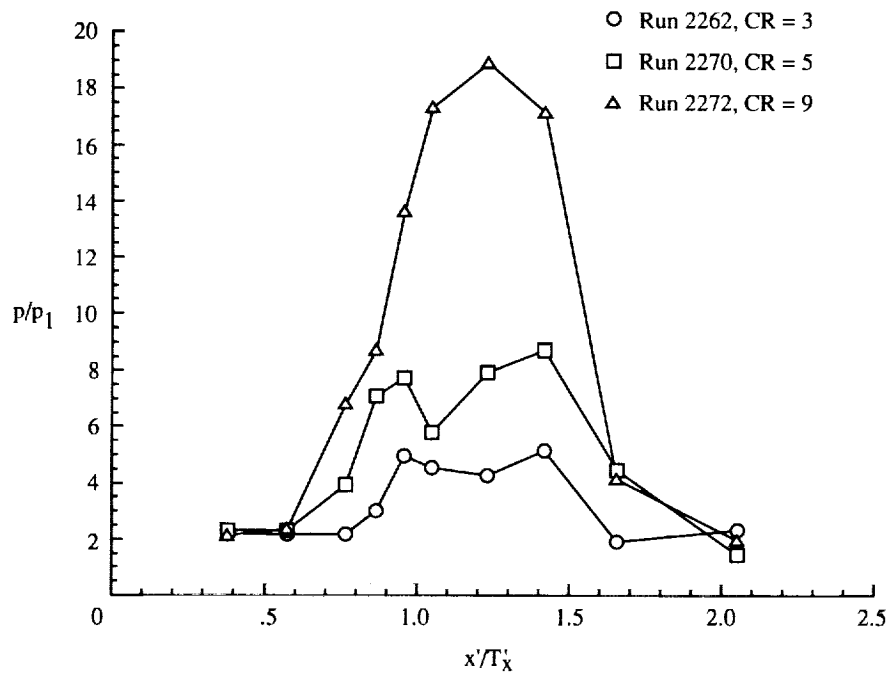


(e) Cowl centerline.

Figure 13. Concluded.

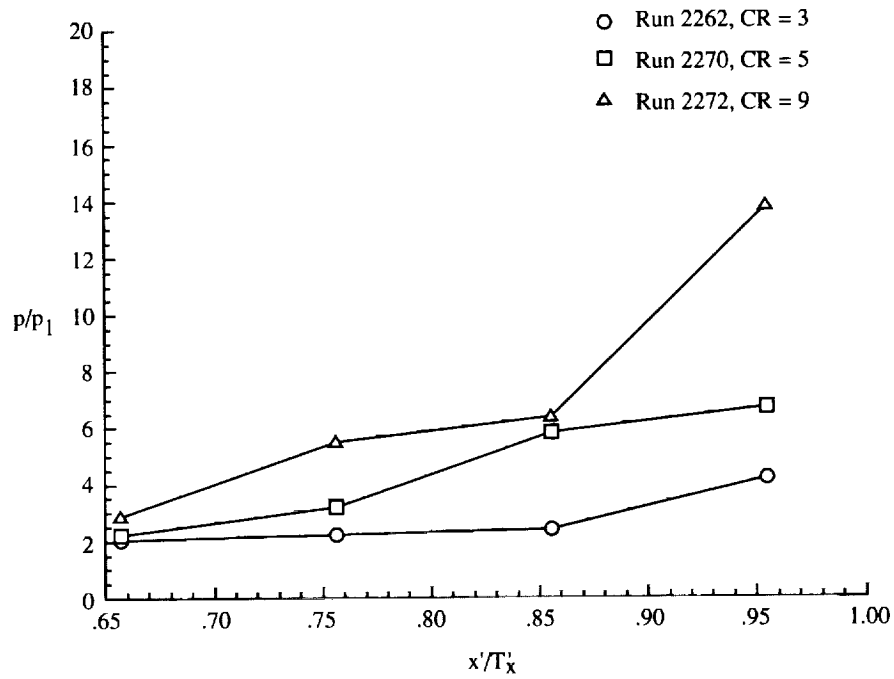


(a) Baseplate centerline.

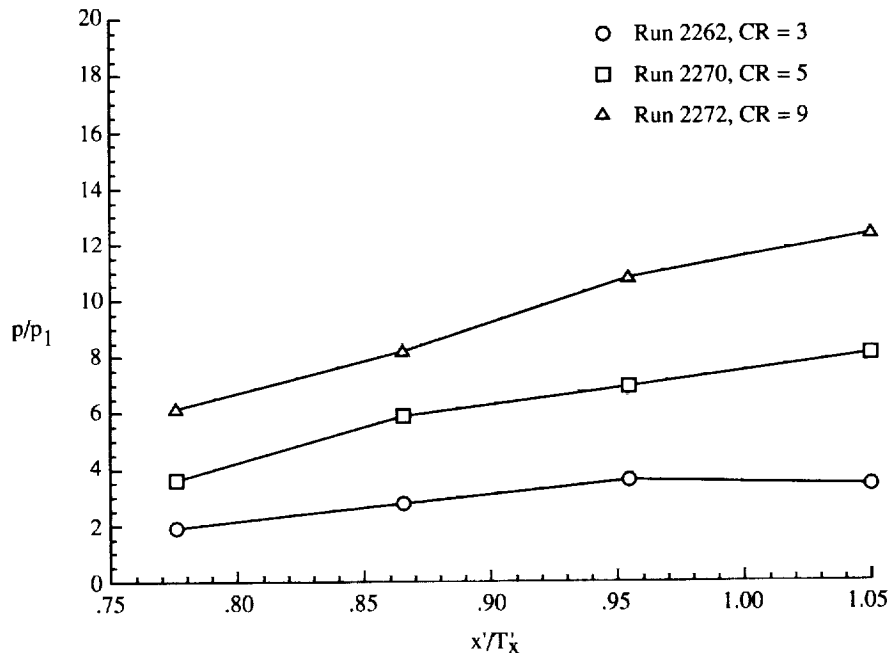


(b) Sidewall centerline.

Figure 14. Contraction ratio effects on pressure distribution. $\Lambda = 30^\circ$; 0-percent cowl; $N_{Re} = 5.50 \times 10^5$ per foot.

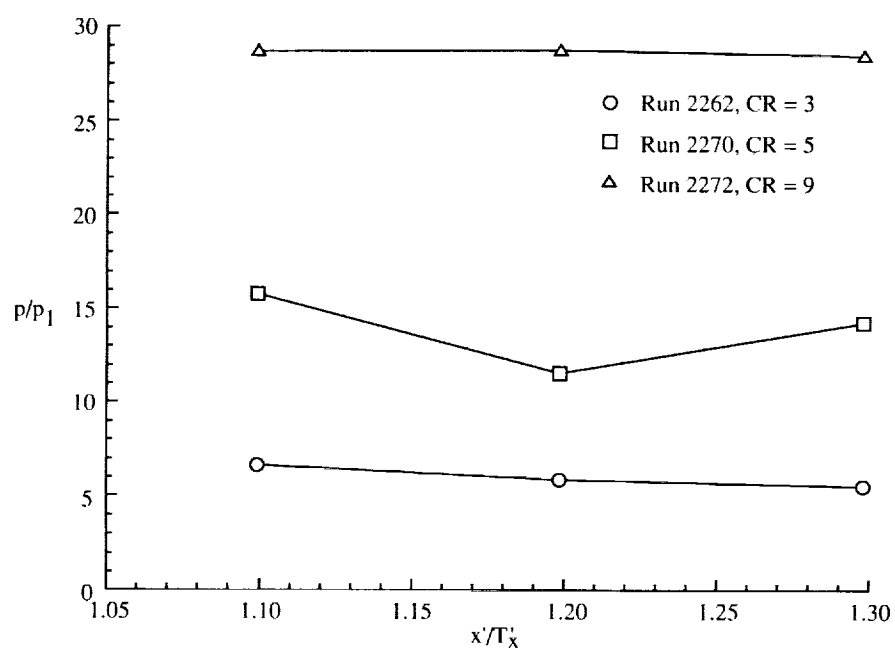


(c) Sidewall at $y/H = 0.13$.



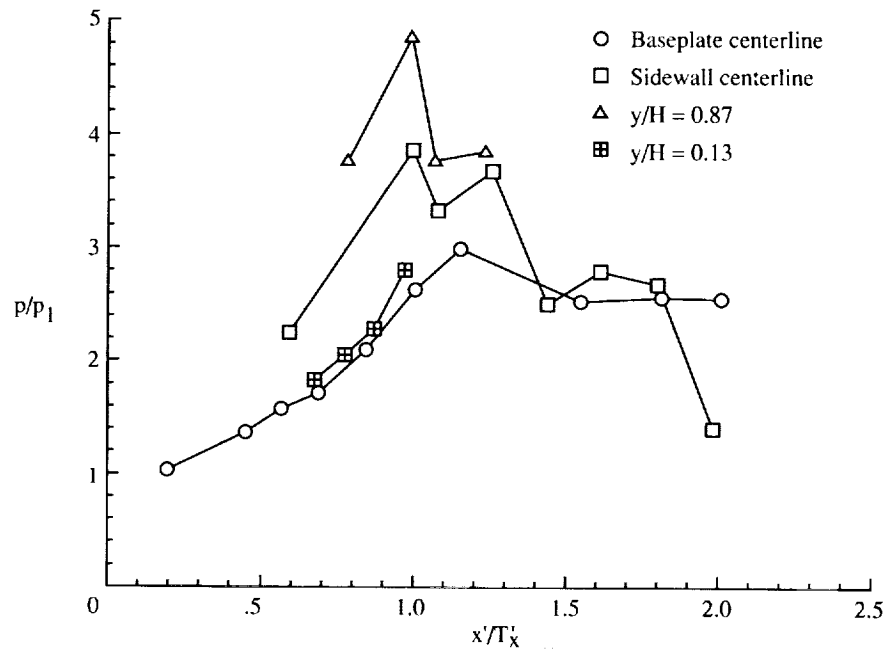
(d) Sidewall at $y/H = 0.87$.

Figure 14. Continued.

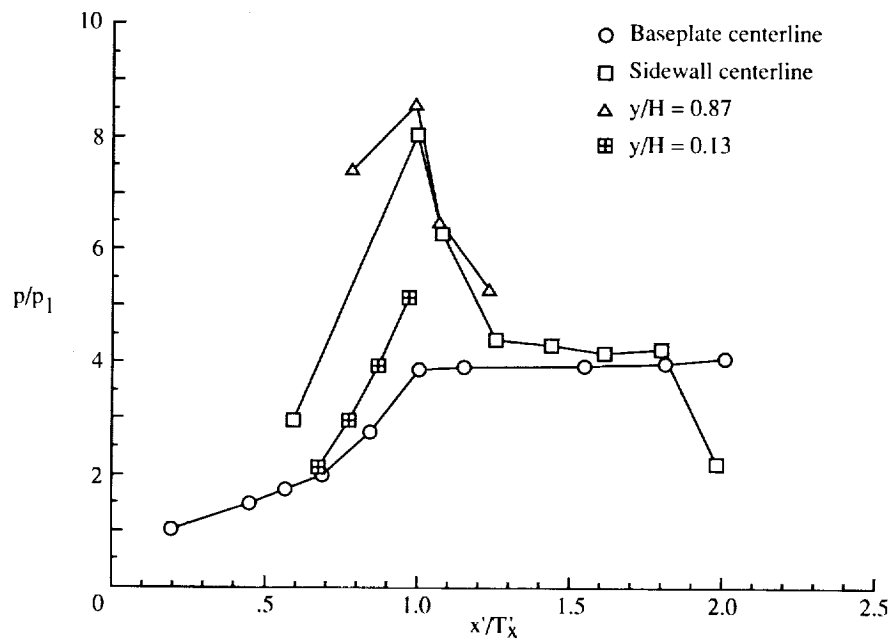


(e) Cowl centerline.

Figure 14. Concluded.

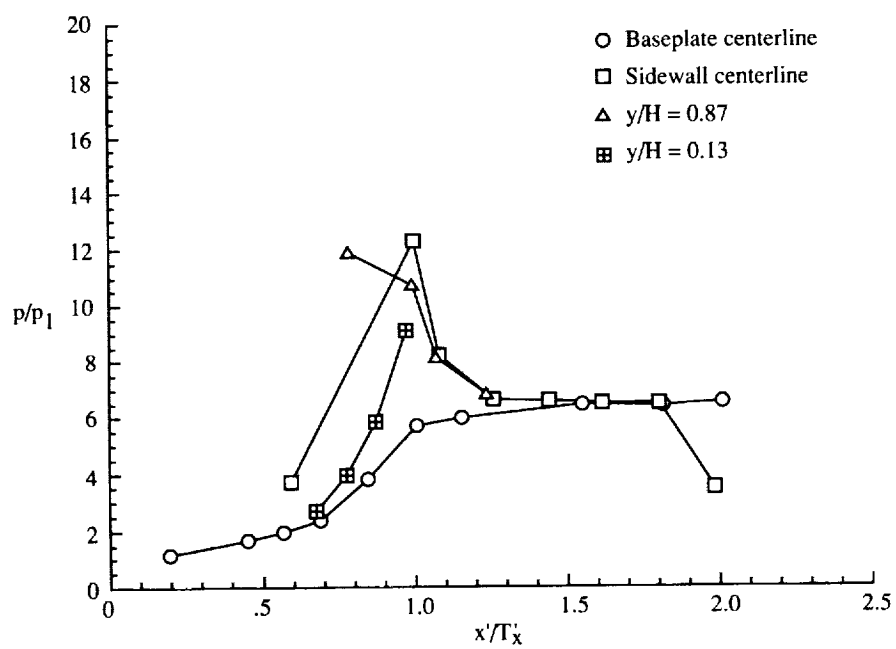


(a) Run 2281; $CR = 3$.



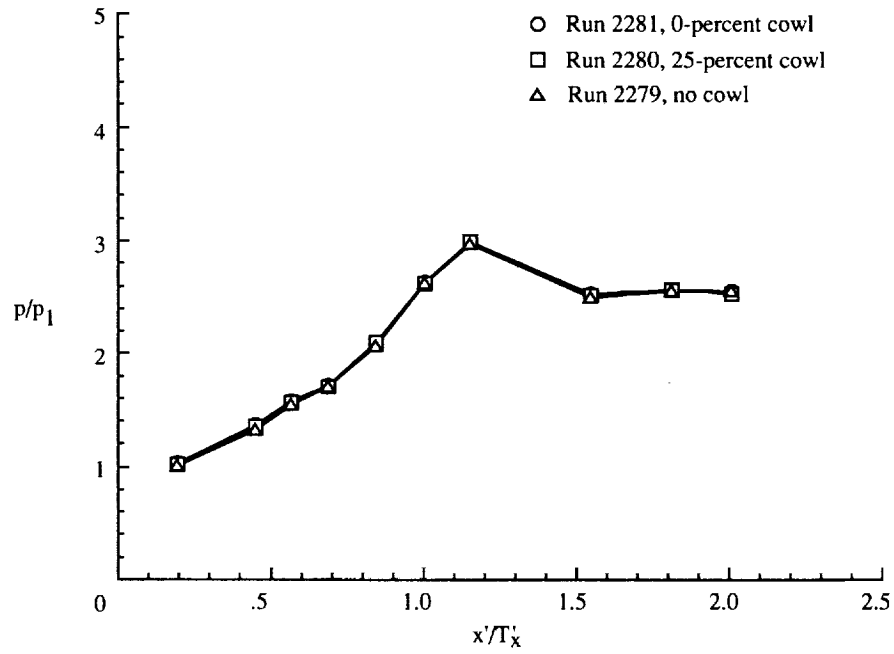
(b) Run 2282; $CR = 5$.

Figure 15. Configuration complete plots for $\Lambda = 70^\circ$, 0-percent cowl, and $N_{Re} = 5.50 \times 10^5$ per foot.

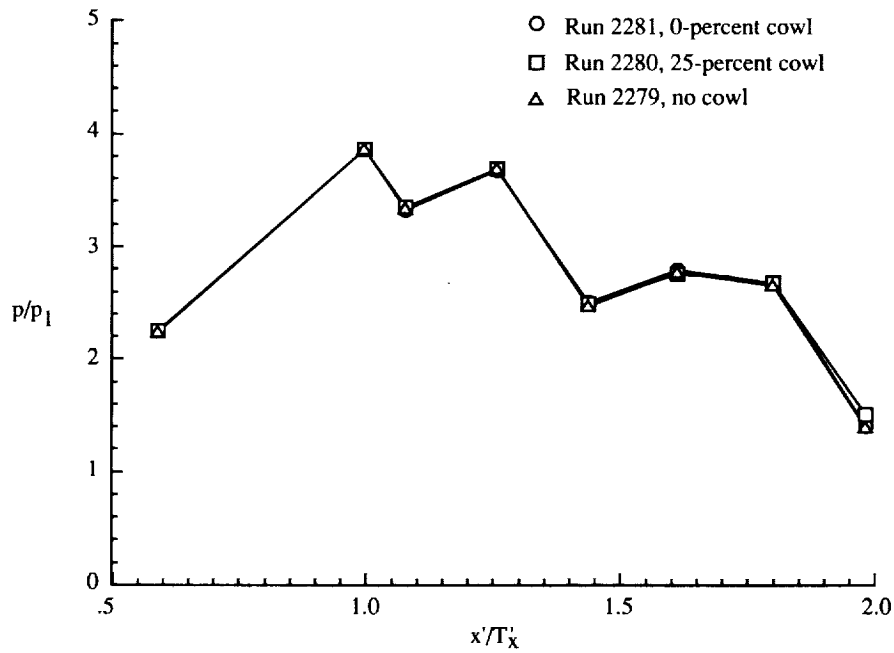


(c) Run 2287; CR = 9.

Figure 15. Concluded.

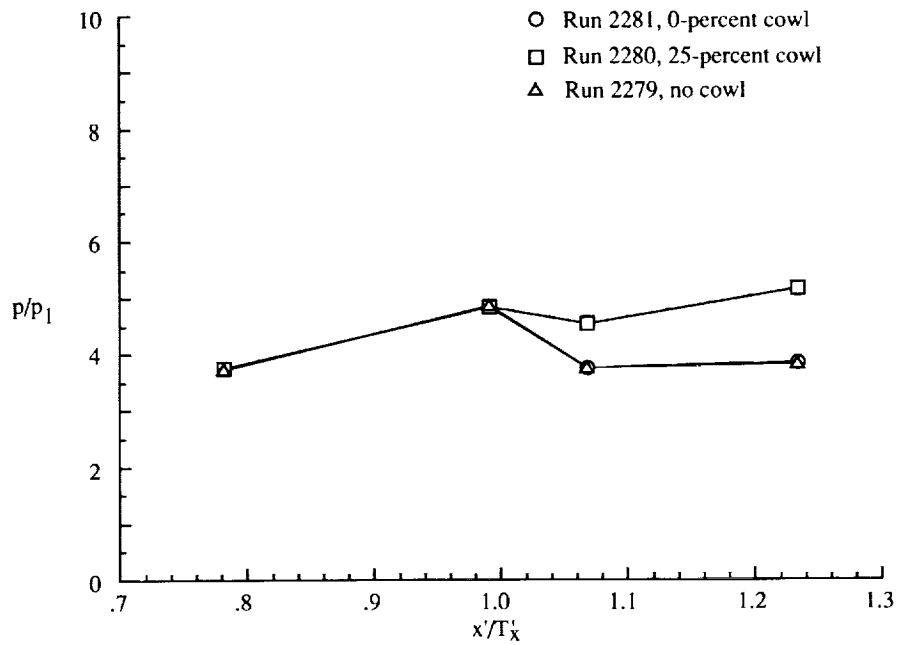


(a) Baseplate centerline.

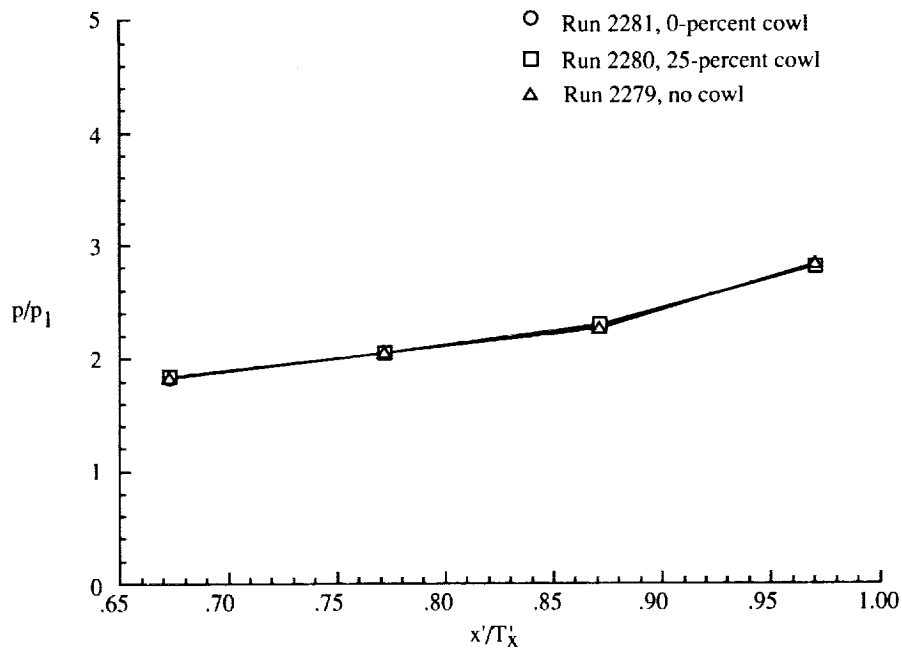


(b) Sidewall centerline.

Figure 16. Cowl effects on pressure distribution. $\Lambda = 70^\circ$; $CR = 3$; $N_{Re} = 5.50 \times 10^5$ per foot.

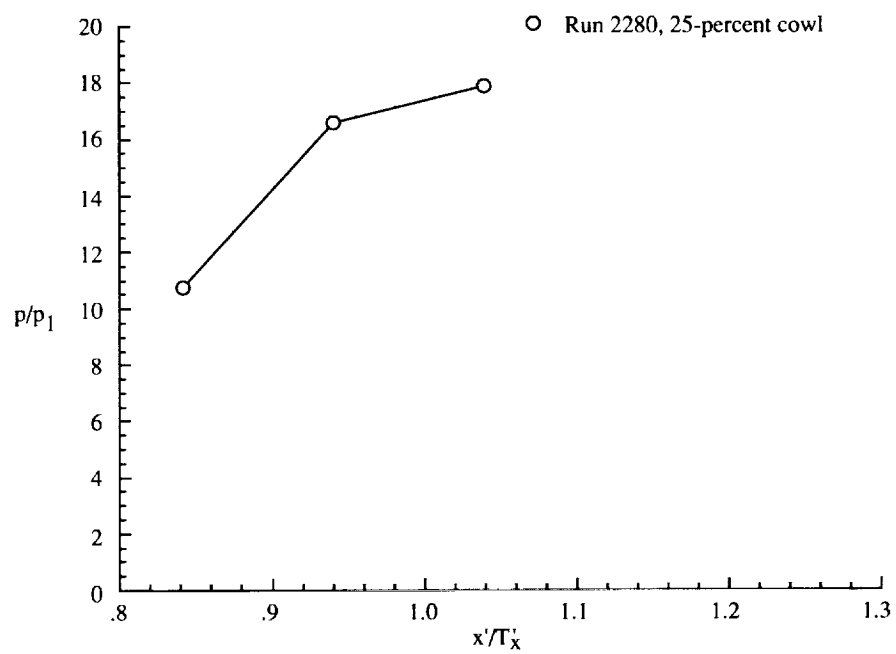


(c) Sidewall at $y/H = 0.87$.



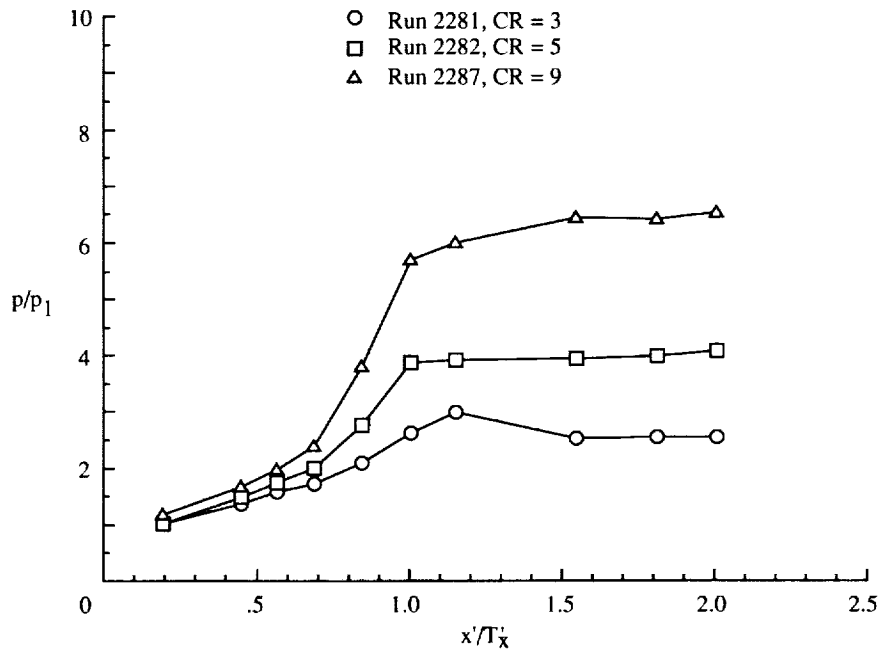
(d) Sidewall at $y/H = 0.13$.

Figure 16. Continued.

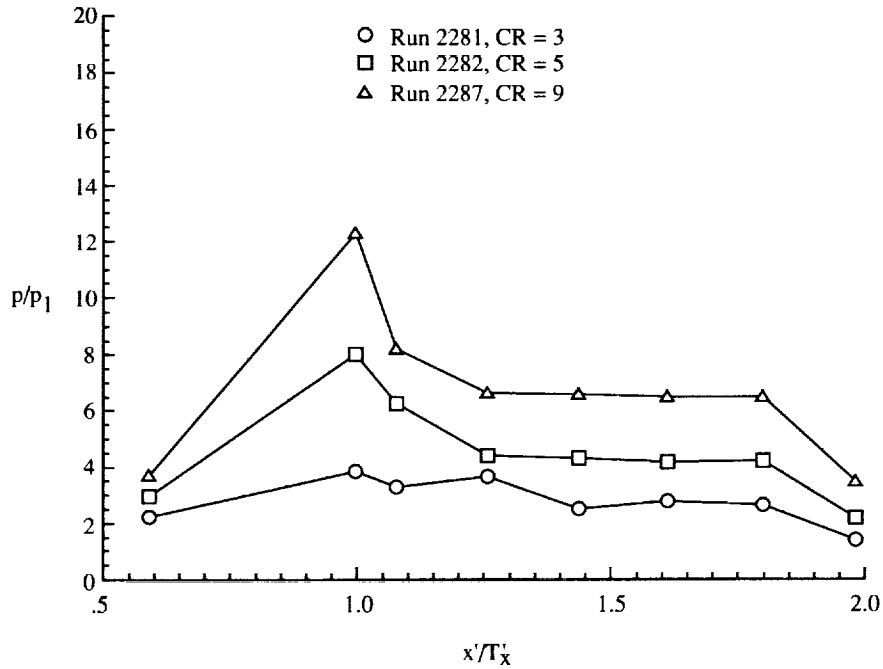


(e) Cowl centerline.

Figure 16. Concluded.

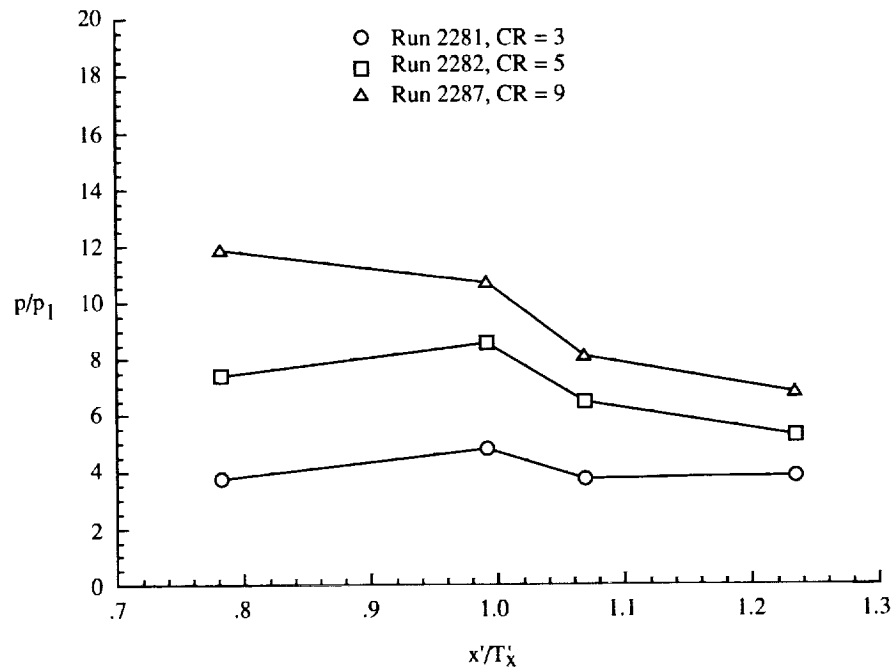


(a) Baseplate centerline.

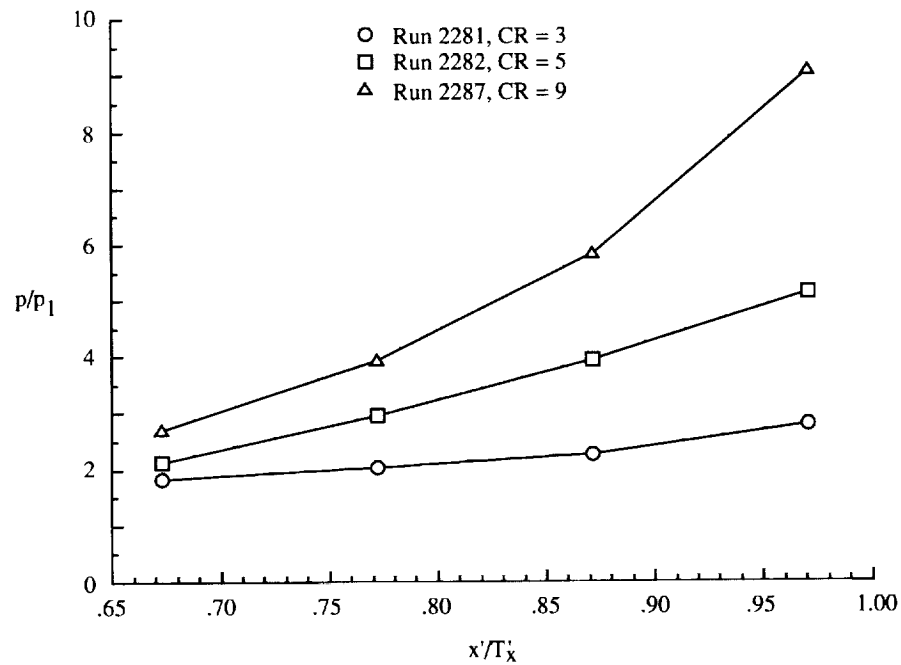


(b) Sidewall centerline.

Figure 17. Contraction ratio effects on pressure distribution. $\Lambda = 70^\circ$; 0-percent cowl; $N_{Re} = 5.50 \times 10^5$ per foot.

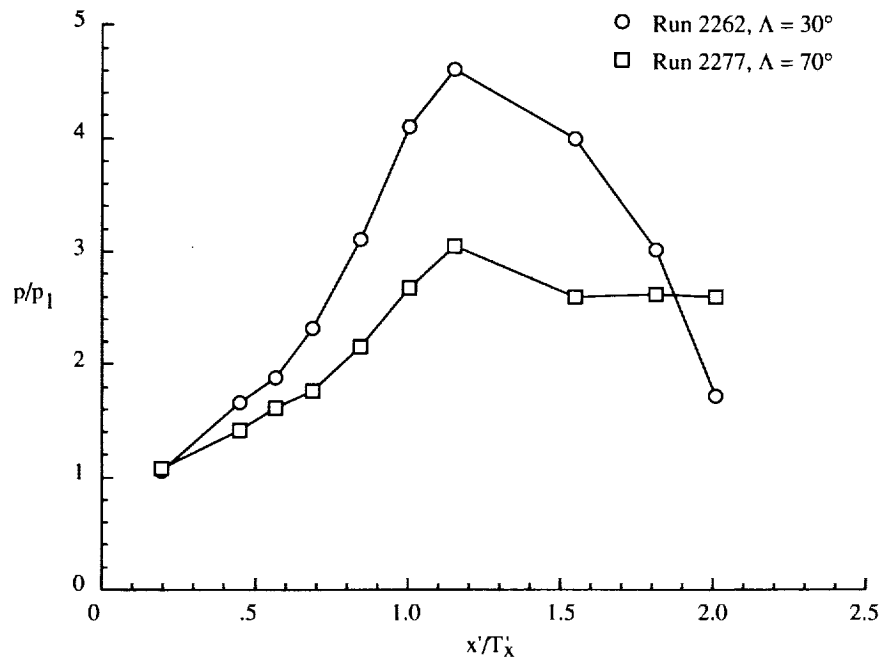


(c) Sidewall at $y/H = 0.87$.

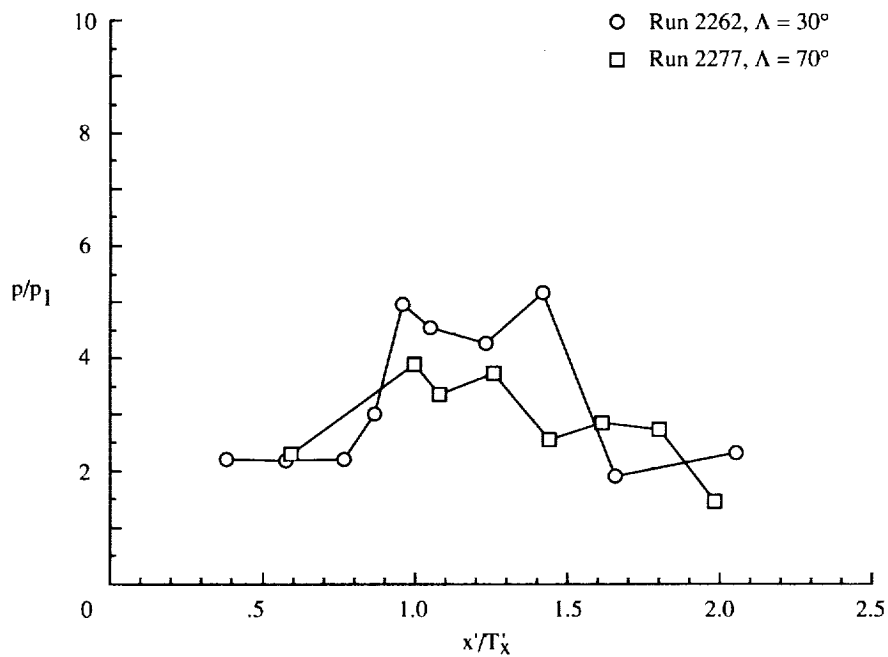


(d) Sidewall at $y/H = 0.13$.

Figure 17. Concluded.

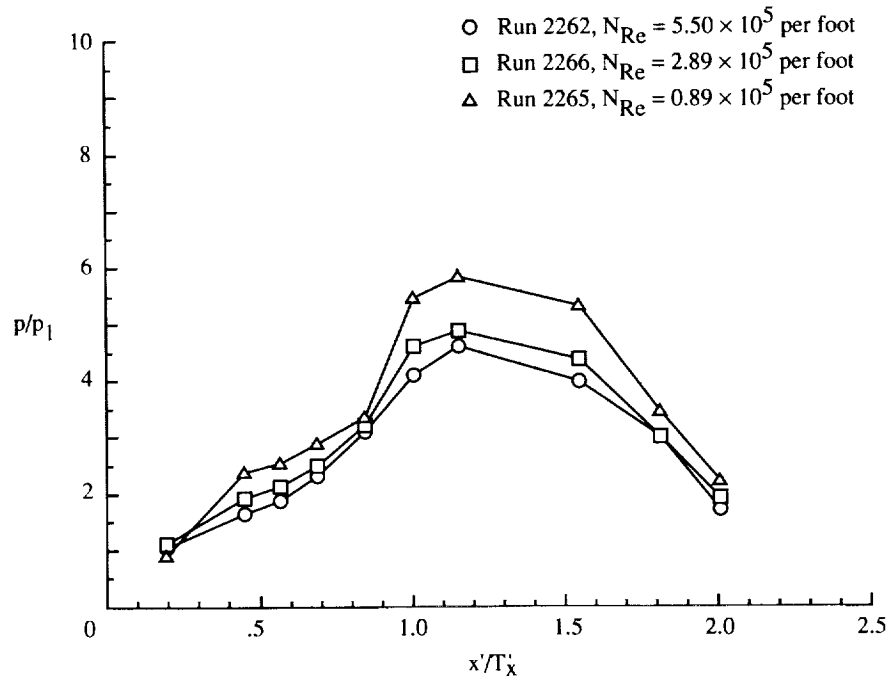


(a) Baseplate centerline.

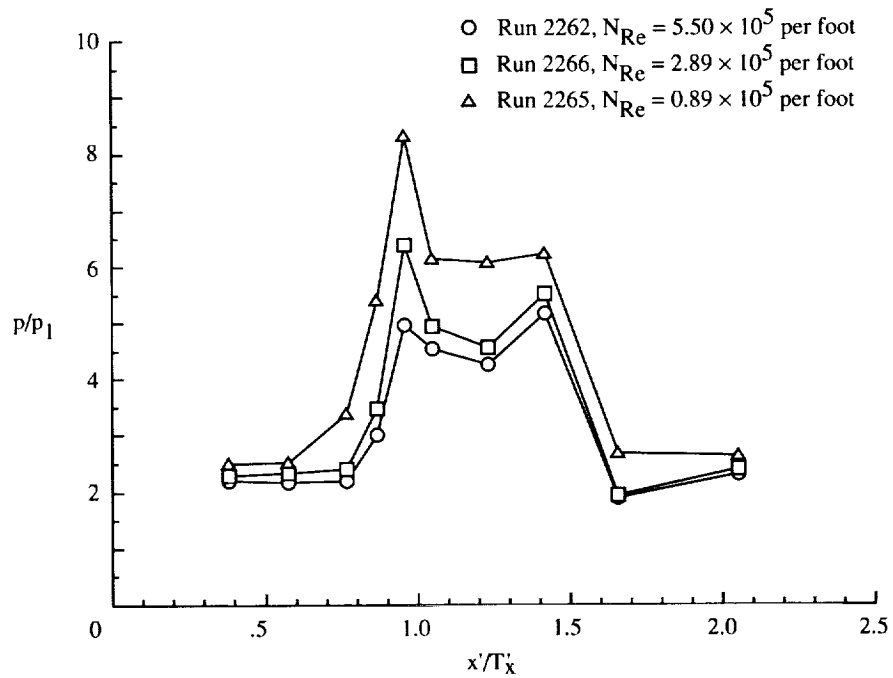


(b) Sidewall centerline.

Figure 18. Leading-edge sweep effects on pressure distribution. $CR = 3$; $N_{Re} = 5.50 \times 10^5$ per foot; 0-percent cowl.

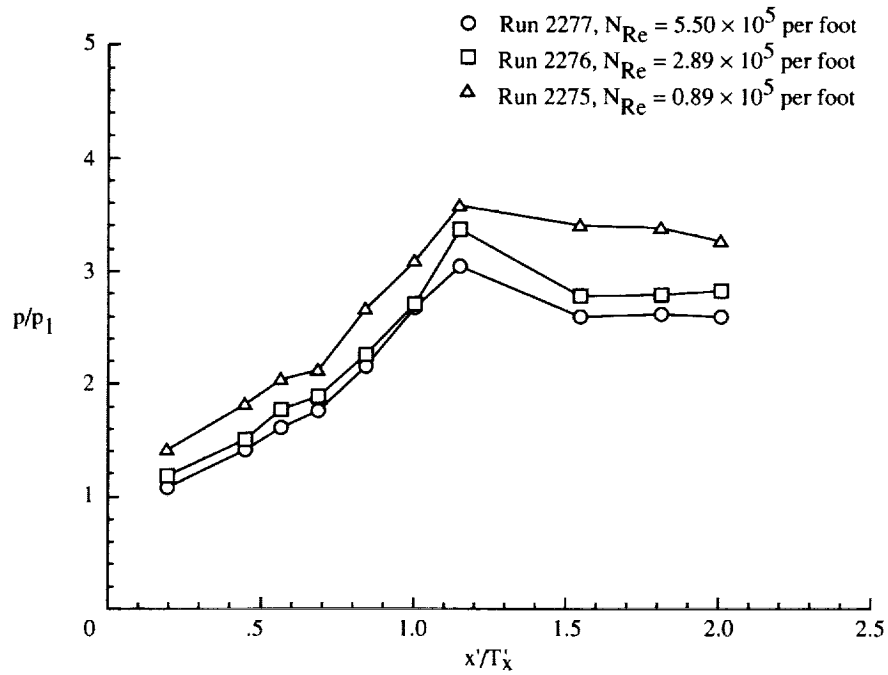


(a) Baseplate centerline.

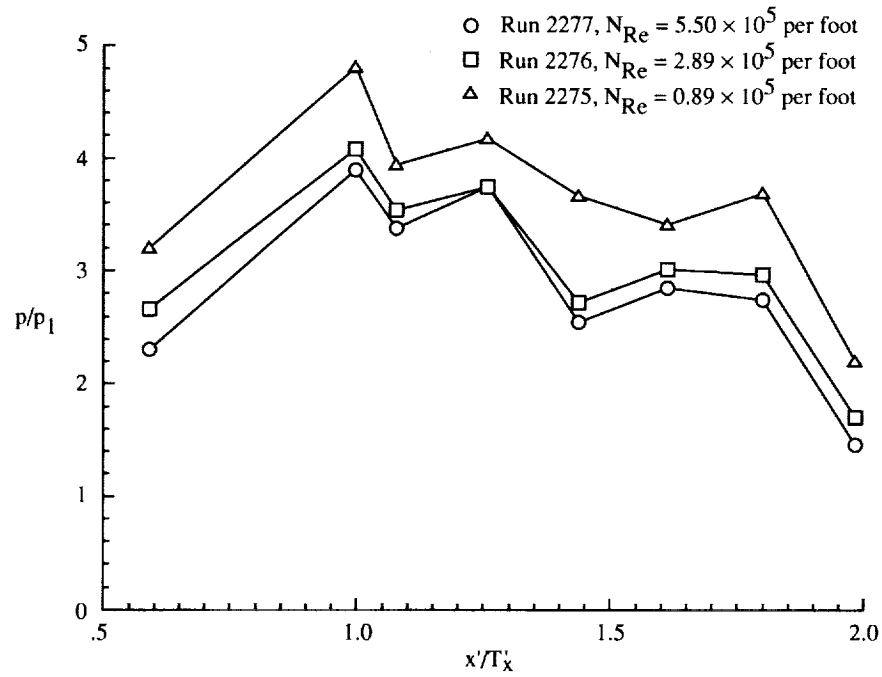


(b) Sidewall centerline.

Figure 19. Reynolds number effects on pressure distribution for $\Lambda = 30^\circ$, $CR = 3$, and 0-percent cowl.



(a) Baseplate centerline.



(b) Sidewall centerline.

Figure 20. Reynolds number effects on pressure distribution for $\Lambda = 70^\circ$, $CR = 3$, and 0-percent cowl.

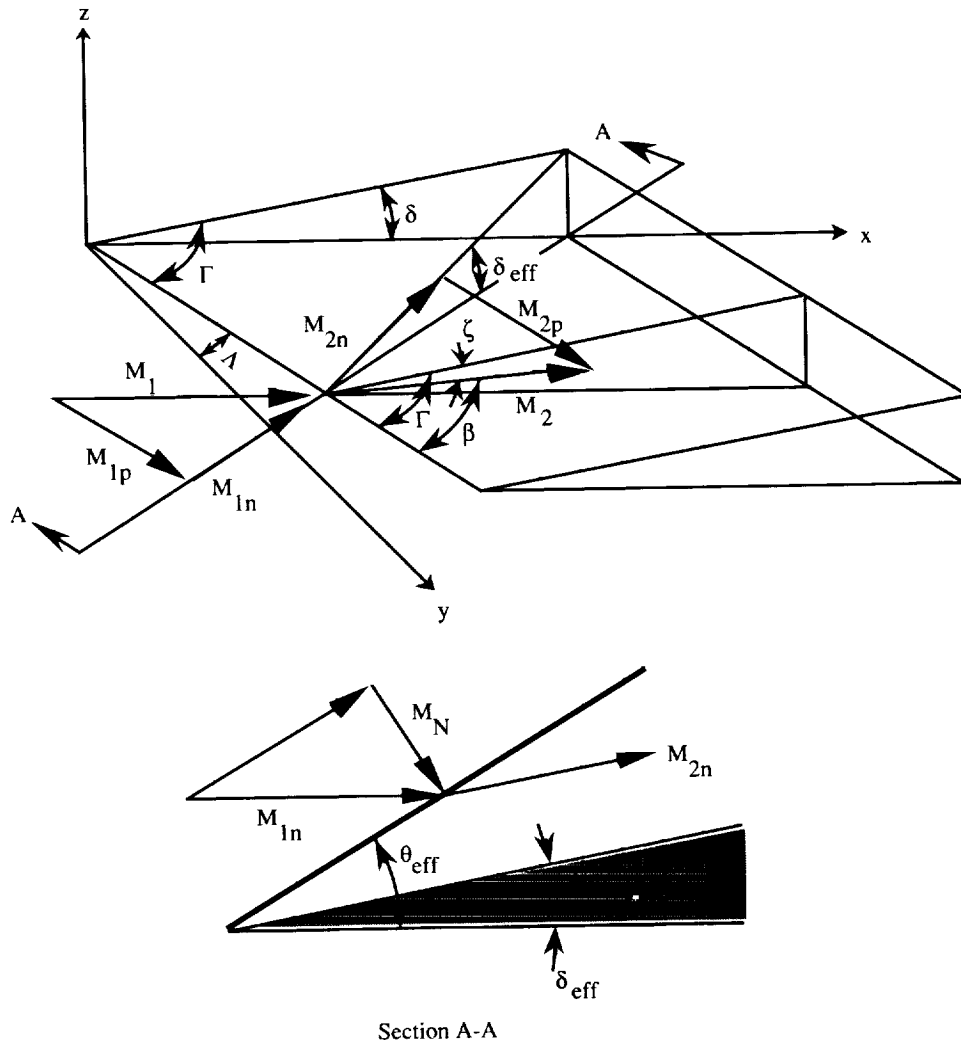


Figure 21. Mach number components for modified two-dimensional oblique shock theory.

REPORT DOCUMENTATION PAGE			Form Approved OMB No. 0704-0188	
Public reporting burden for this collection of information is estimated to average 1 hour per response, including the time for reviewing instructions, searching existing data sources, gathering and maintaining the data needed, and completing and reviewing the collection of information. Send comments regarding this burden estimate or any other aspect of this collection of information, including suggestions for reducing this burden, to Washington Headquarters Services, Directorate for Information Operations and Reports, 1215 Jefferson Davis Highway, Suite 1204, Arlington, VA 22202-4302, and to the Office of Management and Budget, Paperwork Reduction Project (0704-0188), Washington, DC 20503.				
1. AGENCY USE ONLY (Leave blank)	2. REPORT DATE December 1993	3. REPORT TYPE AND DATES COVERED Technical Memorandum		
4. TITLE AND SUBTITLE Experimental Investigation of Generic Three-Dimensional Sidewall-Compression Scramjet Inlets at Mach 6 in Tetrafluoromethane		5. FUNDING NUMBERS WU 506-40-41-02		
6. AUTHOR(S) Scott D. Holland				
7. PERFORMING ORGANIZATION NAME(S) AND ADDRESS(ES) NASA Langley Research Center Hampton, VA 23681-0001		8. PERFORMING ORGANIZATION REPORT NUMBER L-17133		
9. SPONSORING/MONITORING AGENCY NAME(S) AND ADDRESS(ES) National Aeronautics and Space Administration Washington, DC 20546-0001		10. SPONSORING/MONITORING AGENCY REPORT NUMBER NASA TM-4497		
11. SUPPLEMENTARY NOTES				
12a. DISTRIBUTION/AVAILABILITY STATEMENT Unclassified-Unlimited Subject Category 34		12b. DISTRIBUTION CODE		
13. ABSTRACT (Maximum 200 words) Three-dimensional sidewall-compression scramjet inlets with leading-edge sweeps of 30° and 70° have been tested in the Langley Hypersonic CF ₄ Tunnel at Mach 6 and with a ratio of specific heats of 1.2. The parametric effects of leading-edge sweep, cowl position, contraction ratio, and Reynolds number were investigated. The models were instrumented with 42 static pressure orifices that were distributed on the sidewalls, baseplate, and cowl. Schlieren movies were made of each test for flow visualization of the effects of the internal flow spillage on the external flow field. To obtain an approximate characterization of the flow field, a modification to two-dimensional, inviscid, oblique shock theory was derived to accommodate the three-dimensional effects of leading-edge sweep. This theory qualitatively predicted the reflected shock structure (i.e., sidewall impingement locations) and the observed increase in spillage with increasing leading-edge sweep. The primary effect of moving the cowl forward was capturing the flow that would have otherwise spilled out ahead of the cowl. Increasing the contraction ratio increases the number of internal shock reflections and hence incrementally increases the sidewall pressure distribution. Significant Reynolds number effects were noted over a small range of Reynolds number.				
14. SUBJECT TERMS Hypersonics; Inlets; Shock interactions; Tetrafluoromethane			15. NUMBER OF PAGES 46	
			16. PRICE CODE A03	
17. SECURITY CLASSIFICATION OF REPORT Unclassified	18. SECURITY CLASSIFICATION OF THIS PAGE Unclassified	19. SECURITY CLASSIFICATION OF ABSTRACT	20. LIMITATION OF ABSTRACT	